MUON TRIGGER ALGORITHM FOR THE HL-LHC UPGRADE OF THE CMS EXPERIMENT

An Undergraduate Research Scholars Thesis

by

JOSE ROBERTO DIMAS VALLE

Submitted to the Undergraduate Research Scholars Program
Texas A&M University
in partial fulfillment of the requirements for the designation as an

UNDERGRADUATE RESEARCH SCHOLAR

Approved by
Research Advisor: Prof. Alexei Safonov

May 2016

Major: Physics and Astronomy

TABLE OF CONTENTS

ABSTRACT

Muon Trigger Algorithm for the HL-LHC Upgrade of the CMS Experiment

Jose Roberto Dimas Valle
Department of Physics and Astronomy
Texas A&M University

Research Advisor: Prof. Alexei Safonov
Department of Physics and Astronomy

After the successful discovery of the Higgs Boson at the Large Hadron Collider (LHC), efforts have shifted toward the understanding of the dynamic behind the Higgs mechanism and the implied consequences that can further extend the Standard Model of Particle Physics. One class of models of new physics implies existence of "hidden" sectors of particles, some of which could be produced at the upgraded LHC. In many scenarios, such particles may have an appreciable lifetime and can decay to pairs of muons leading to signatures with muon pairs produced away from the beamline. However, existing muon trigger algorithms show large inefficiencies for detecting such muons. Therefore, we propose and investigate a conceptually new trigger algorithm for reconstructing and measuring momenta of displaced muons using information from muon spectrometers only, which can be implemented as part of the re-design of the CMS Level-1 muon trigger for the HL-LHC to maintain CMS sensitivity to signatures with displaced muons.

ACKNOWLEDGMENTS

I would like to acknowledge Dr. Alexei Safonov and Dr. Vyacheslav Krutelyov for their support and guidance on the completion of this Undergraduate Research Scholars Thesis.

Dr. Duncan MacKenzie for his commitment and devotion in projects involving undergraduate students and for his successful leadership of the Undergraduate Research Scholars Program.

Special thanks to Yuriy Pakhotin, Aysen Tatarinov, Sven Dildick and Tao Huang for all of their help during my research.

CHAPTER I

INTRODUCTION

I.1 Standard Model and Beyond

The Standard Model (SM) of particle physics explains the interactions of known subatomic particles [1-3]. It accounts for electromagnetic, weak and strong interactions. Fig. I.1 shows the building blocks of the model, leptons such as electrons and neutrinos, quarks, which finally agglomerate to yield composite particles, and gauge bosons, which are carriers of interactions. The list for elementary particles was updated to include the recently discovered Higgs Boson [4-8]. Detailed review of the SM can be found elsewhere [9].

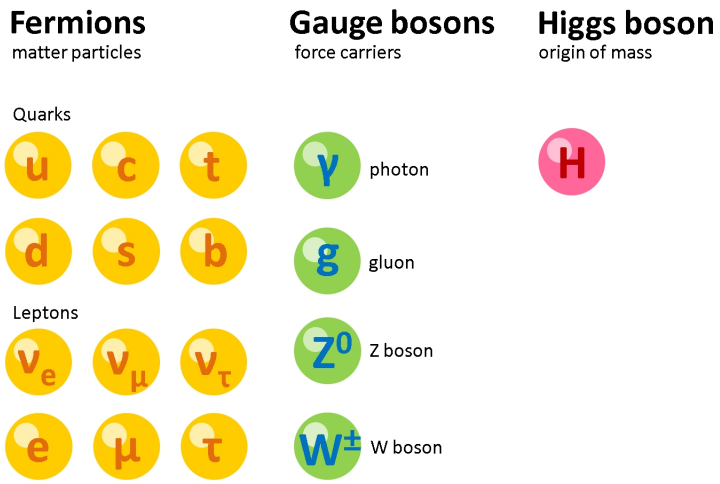

Fig. I.1. Elementary particles: leptons, quarks and gauge bosons [10].

Fig. I.2 shows the distribution of the invariant mass of four muons in CMS data showing a distinct peak, illustrating the discovery of a new particle with invariant mass around 126 GeV reconstructed from two pairs of leptons, a predicted signature into which the Higgs boson decays.

The Standard Model gives specific predictions for the final states the Higgs boson can decay into. However, a number of the theories suggest additional final states, including a number of models predicting decays of the Higgs boson to pairs of new bosons (not necessarily exclusively), which

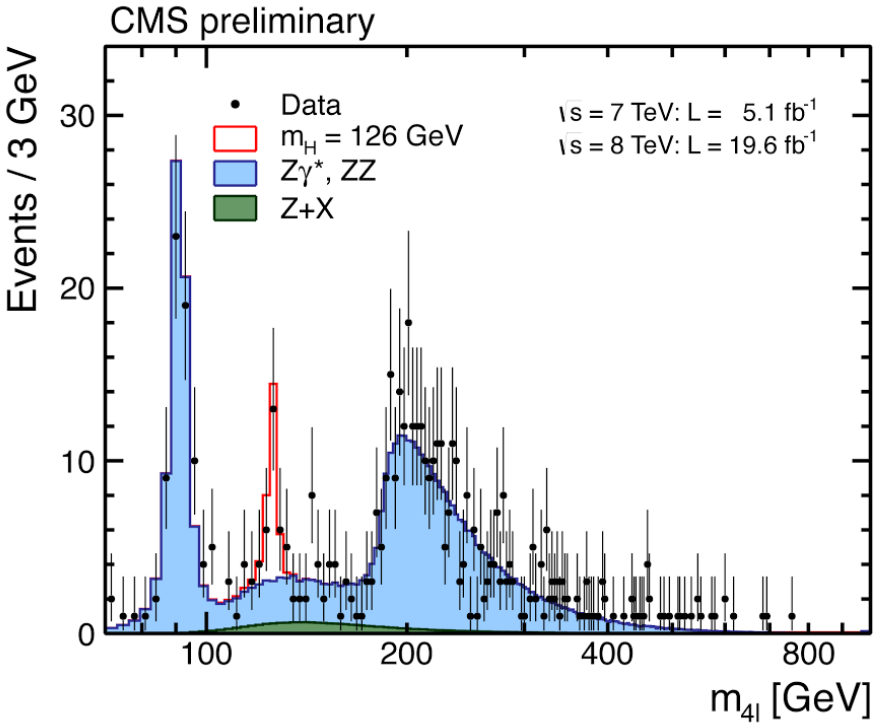

Fig. I.2. Higgs signal observed by the CMS experiment as an excess of 4 leptons events at a mass of 126 GeV (red peak) [7].

may in turn decay to pairs of muons. Frequently, these new bosons are predicted to have an appreciable lifetime leading to decays that happen between 10 to 100 cm away from the beamline.

This neutral particle will leave no imprints in the tracker detector but its final products will likely be detected in muon system. However, successful triggering on such muons required good detection efficiency and momentum reconstruction that properly take into account the displacement of the mother particle before decaying. Such displaced muons signatures are considered important elements of the CMS physics program as they could hold keys for dark matter, baryon abundance, matter-antimatter asymmetry and other phenomena not explained by the Standard Model. Fig. I.3 shows one of such decays from the Higgs ending with muons.

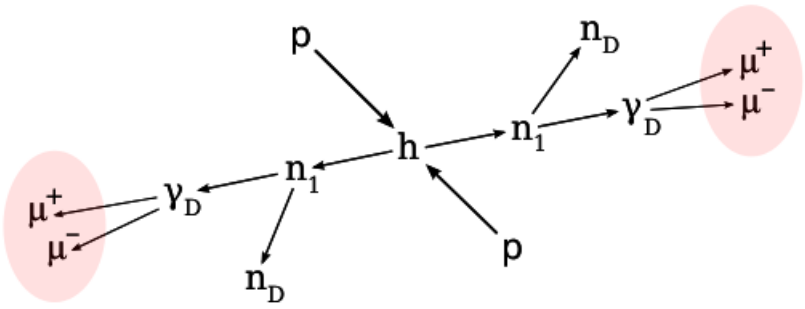

Fig. I.3. One of the proposed chain decays of the Higgs boson than create a long lived neutral particle with muons as the final products.

I.2 Large Hadron Collider

The Large Hadron Collider (LHC) is an international project oriented to the discovery of the particle responsible for the electroweak symmetry breaking (Higgs boson) as well as searches for new phenomena beyond the Standard Model. The LHC collider is a ring of 27 km of circumference that's used to accelerate protons up to highly relativistic speeds. At the LHC design energies at the center of mass of 14 TeV and intensities in excess of 10^{34} cm^{-2}s^{-1}, the particle beams travel in opposite directions inside the ring until they collide, 40 million times per second, in specifically designed points where the beams are directed to cross each other.

There are seven detectors located at these crossing points. Two of the largest experiments, the Compact Muon Solenoid (CMS) and A Toroidal LHC ApparatuS (ATLAS), are general purpose detectors that confirmed the existence of the Higgs boson. The general view of the LHC and the detectors can be found in Fig. I.4. Search for the Higgs boson, tests of the Standard Model and searches for new physics signatures motivated the construction of the biggest particle accelerator in the world. After the first run of the LHC in 2012, the collider went to a long shutdown period before restarting its operations in 2015. The center of mass energy has increased from 8 TeV to 13 TeV and the luminosity up to 2x10^{34} cm^{-2}s^{-1}.

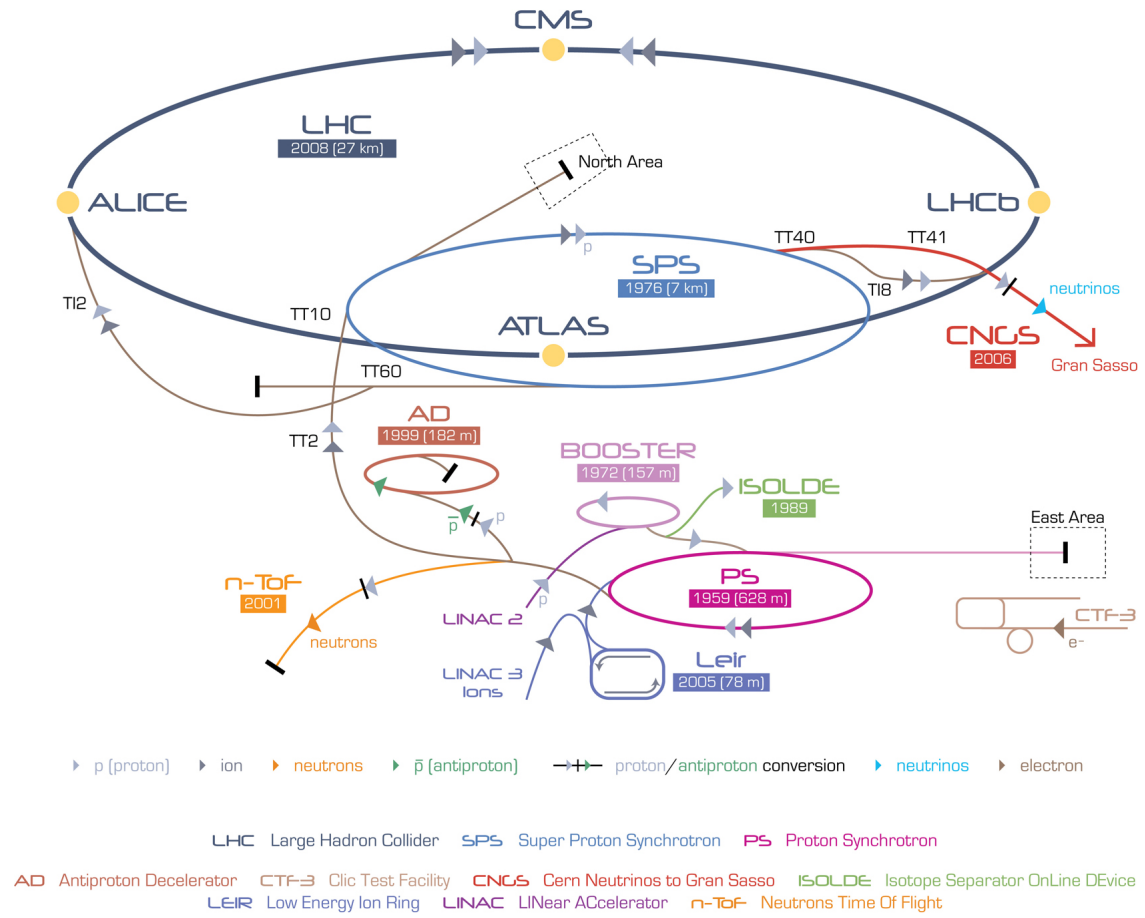

Fig. I.4. Large Hadron Collider (LHC) at CERN [11].

I.3 CMS Experiment

The Compact Muon Solenoid (CMS) detector is a general purpose particle detector designed for precision measurements of the products coming from proton proton collision. The core of the detector is a solenoid whose 3.8 T magnetic field bends charged particles as they traverse inside the detector hitting multiple layers of detection.

As it can be seen in Fig. I.5, the innermost layers are reserved for the silicon tracker that detects charged particles and registers their momentum. After the tracker, the electromagnetic and hadron calorimeters stop most of the particles and measure their energy. The magnetic solenoid is placed

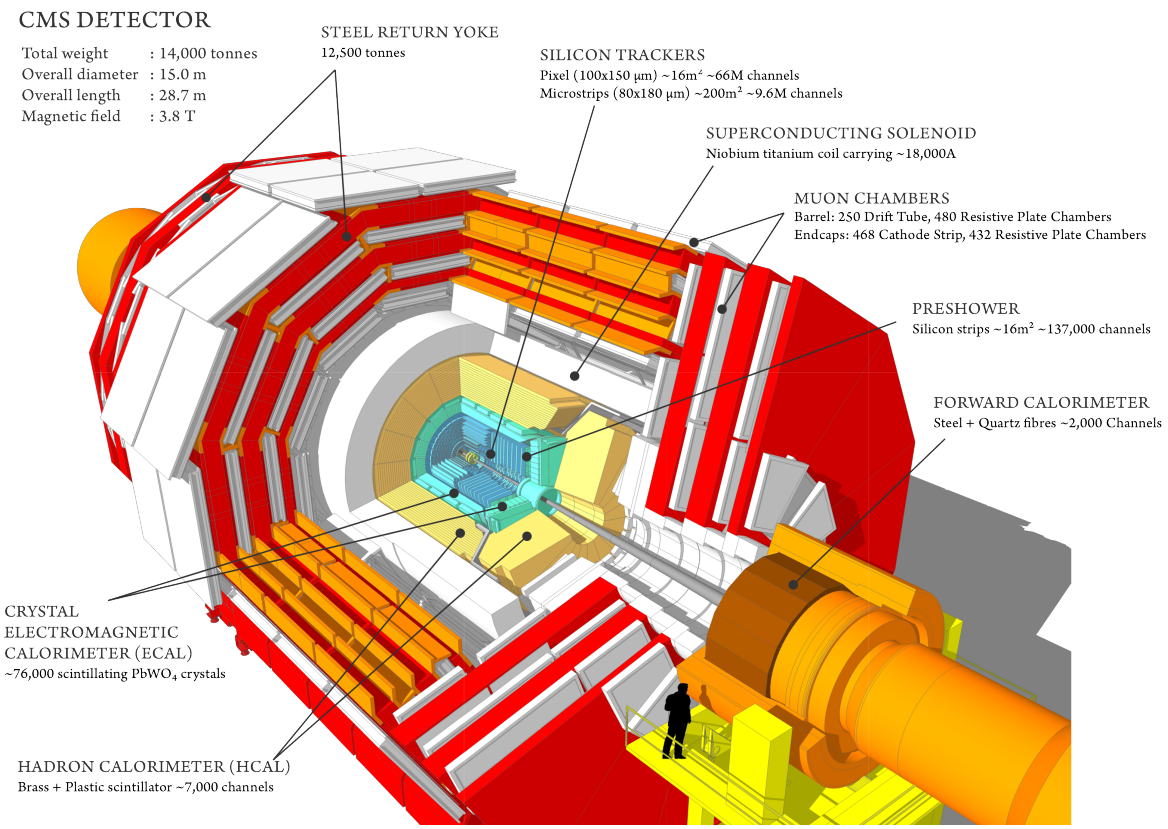

Fig. I.5. Overall disposition of the CMS experiment showing the different layers of detection. The black silhouette of a man is for comparison of the size [13].

around the calorimeters and provides a constant magnetic field. The muon spectrometer is placed at the outermost layer in the detector because muons can nearly freely pass through significant amount of matter.

The CMS registers information from the silicon tracker, the electromagnetic and hadron calorimeters and the muon system in order to reconstruct the collision events at the crossing point. An illustration of event reconstruction is shown in Fig. I.6 displaying a candidate event possibly coming from a Higgs decay into a pair of Z bosons followed by a decay of each Z boson to pairs of muons.

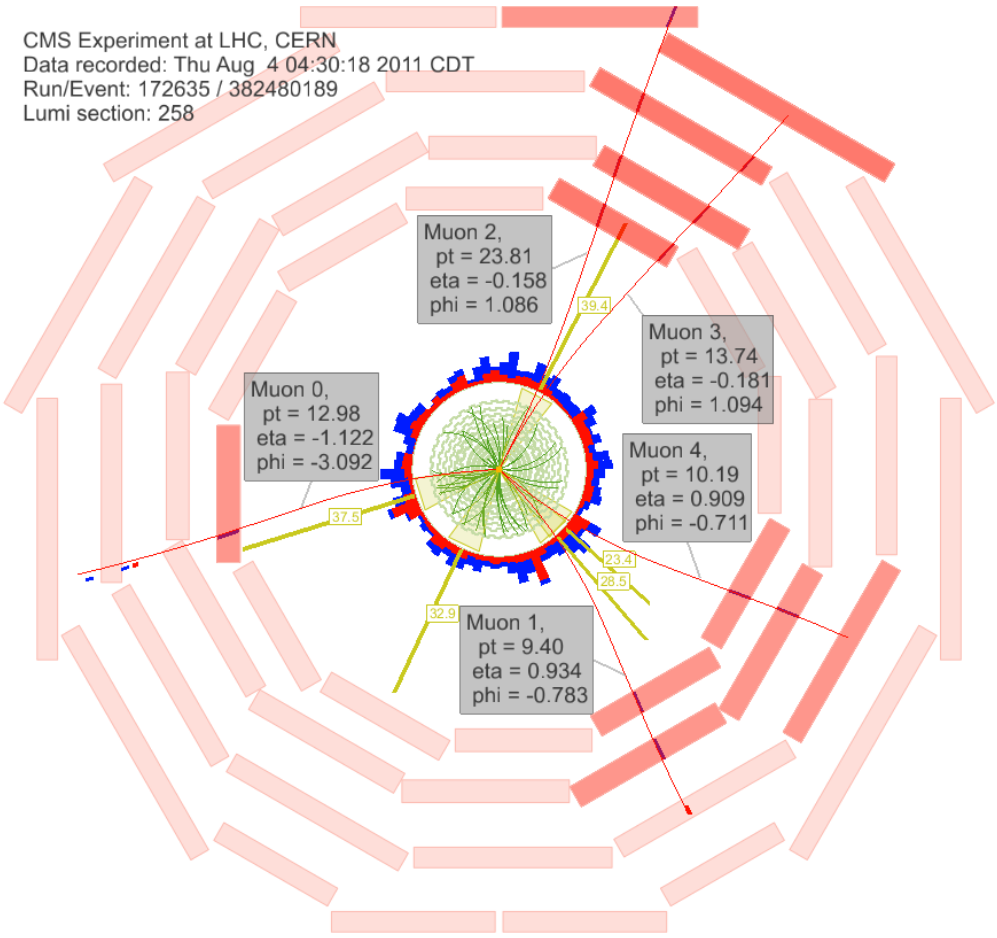

Fig. I.6. Example of an event reconstruction using the DT muon system (light red) in the barrel region of the CMS detector as well as the calorimeters (red and blue towers) and the silicon tracker (green tracks). If the event satisfies the triggering requirement, the information information is stored for offline analysis [12].

The muon system is a cylindrical shaped arrangement of detection chambers surrounded by a return yoke for the magnetic field. It is composed of the barrel and endcap regions. The barrel region relies on the Drift Tubes (DT) detectors while the endcaps use Cathode Strip Chambers (CSC) for track measurements. Both regions also use Resistive Plate Chambers (RPC) to assist with triggering. Future upgrades include the addition of Gas Electron Multiplier (GEM) chambers in the endcap and overall faster electronics for the whole CMS detector [14]. At high luminosity, the

information generated by the CMS detector adds up to 1-2 MB per collision event. At a rate of 40 million collisions per second the amount of information adds up to 76 TB of data per second. That is enough information to stack a 50 m pile of Blu-ray discs every single second. However, most of the collision events do not represent any new or interesting physics discoveries and can be discarded safely, if such events could be recognized online.

The trigger system is designed to perform an ultra-fast selection of potentially interesting events to diminish the rate of data to the level at which the data can be written to disk for offline analysis, reducing the number of events from 40 million to just hundreds of events per second. This is done by recognizing events that carry potentially interesting new physics, for example requiring high energy muons as well as information from the tracker and calorimeters. The energy can be measured by reconstructing the transverse momentum of a particle, which is the momentum perpendicular to the beam line, and applying selections to get rid of non interesting events.

We discuss the functionality of the CMS muon system and analyze the basis of its performance in further detail in Chapter II.

However, currently available triggering algorithms discard most of the displaced muons because of a mismeasurement of the transverse momentum. We discuss the performance of the current algorithm as well as their potential shortcomings in Chapter III.

We propose and study an algorithm that performs appropriately for both displaced and prompt muons using information of the muon system alone in Chapter IV.

Finally, we present the conclusions drawn from this undergraduate scholar research.

CHAPTER II

MUON DETECTOR OF THE CMS EXPERIMENT AT THE LHC

The muon system is a cylindrical shaped arrangement of detection chambers surrounded by a return yoke for the magnetic field. It is composed of the barrel and endcap regions. The barrel region relies on the Drift Tubes (DT) detectors while the endcaps use Cathode Strip Chambers (CSC) for track measurements. Both regions also use Resistive Plate Chambers (RPC) to assist with triggering as shown in Fig. II.1. The existence of several layers of muon detectors (muon stations) ensures the reliability and redundancy of the system. In this chapter we explain the general functionality of the detector algorithm used to reconstruct the track of a muon and produce a rough measurement of its momenta and angular position inside the detector.

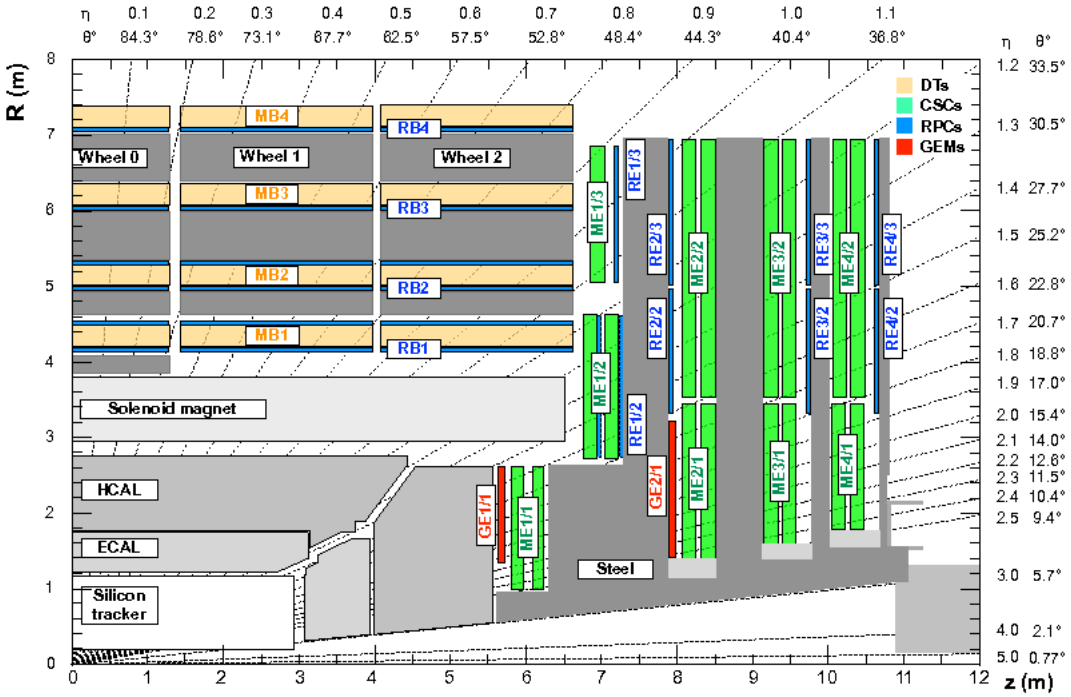

Fig. II.1. Muon System of the CMS experiment. Barrel region is composed of Drift Tubes (DT), while the Endcap Regions are composed of Cathode Strip Chambers (CSC). Resistive Plate Chambers (RPC) are present in both regions. Gas Electron Multiplier (GEM) are installed in the high η region only. [16].

II.1 Lorentz Force and Magnetic Bending

As it was shown in Fig. I.5, the shape of the CMS detector is best described using cylindrical coordinates. Fig. II.1 shows a longitudinal cut of the detector showing cylindrical R and z coordinates. The ϕ coordinate is the traditional azimuths angle in cylindrical coordinates. Fig. II.1 shows another useful coordinate: the polar angle, θ, measured from a line perpendicular to the beamline. However, since the differences in θ are not Lorentz invariant, we define a quantity, called the *pseudorapidity* as follows:

$$\eta \;=\; -\ln\left[\tan\frac{\theta}{2}\right].$$

The use of the pseudorapidity comes from its relationship to the momentum of a particle given by:

$$\eta \;=\; \frac{1}{2}\ln\frac{|\vec{p}|+p_L}{|\vec{p}|-p_L} = \tanh^{-1}\frac{p_L}{|\vec{p}|},$$

Where $|\vec{p}|$ is the magnitude of the momentum and p_L is longitudinal momentum, i.e. the component of the momentum along the beam axis. The magnetic field is provided by a 3.8 T solenoid, which is responsible for the bending of the particles inside the detector. The force acting on a charged particle is given by the Lorentz force:

$$\vec{F} \;=\; q\frac{\vec{p}}{m}\times\vec{B},$$

where q is the charge of the particle, $\vec{p}$ is its momentum, m is its mass and $\vec{B}$ is the magnetic field which is causing the force $\vec{F}$ that bends trajectory of the particle. The expression $\vec{p}\times\vec{B}$ can also be written as $p_T * B_L$, where p_T is the transverse momentum of the particle relative to the beamline, and B_L the longitudinal component of the magnetic field, i.e. the component parallel to the beamline. The strongest component of the magnetic field points along the z axis, therefore most of the bending will be reflected on the ϕ coordinate. The radius of curvature of the bending of the trajectory can be related to the transverse momentum as follows:

$$|\vec{r}| \;=\; \frac{\vec{p}\times\vec{B}}{q|\vec{B}|^2} = \frac{p_T * B_L}{qB^2}.$$

Therefore, low p_T muons will have smaller radius of curvature and more pronounced bending. High p_T muons will have larger radius of curvature and therefore will travel in almost straight lines. This is the basic principle of operation for measuring the p_T.

The muon system was designed to be very sensitive in the ϕ coordinate, having a resolution $\Delta\phi$ of about 0.75 mrad. This allows us to reconstruct the transverse momenta of muons with high precision.

Fig. II.2 shows the distribution of the magnetic field in the CMS detector. The magnetic field is very uniform and almost constant in the Barrel but it varies considerably and weakens in the Endcap Regions where it starts to bend in the radial direction. Muon paths are affected by these changes and special care has been taken to reduce mismeasurements due to the non uniformity of the field.

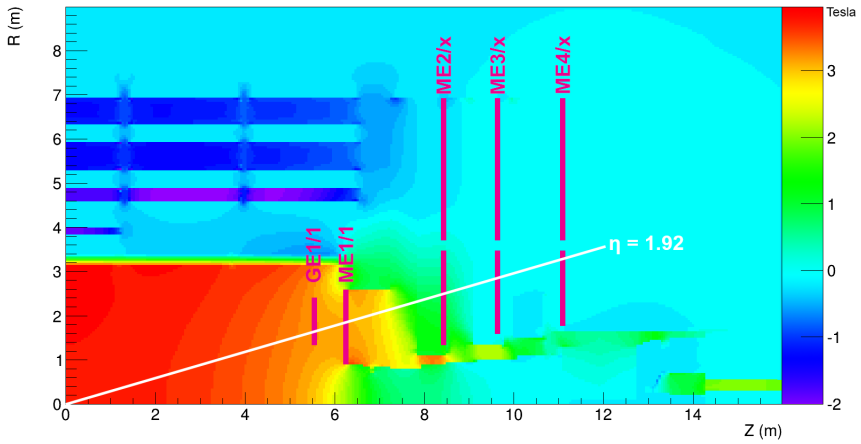

Fig. II.2. Magnetic Field Map of the solenoid in the CMS experiment. [16].

II.2 Barrel Region of the CMS experiment

The Muon detector in Barrel region (MB) has 240 chambers built using Drift Tubes arranged in four concentric stations MB1, MB2, MB3 and MB4. It is divided into five wheels of twelve sectors (in stations 1-3 and fourteen sectors in station 4) of roughly 30° in ϕ coverage each. To avoid pointing cracks between sectors, chambers in different stations are staggered. Station MB4 is special as it has almost 100% acceptance because of the modules being installed like shingles around the outside of the detector. The only dead area is near the supporting feet. Stations MB1 and MB2 are arranged in such a way that a muon always crosses at least one of them. The arrangement of MB3 with respect to MB1 and MB2 ensures that every muon escaping the barrel crosses at least 3 stations. Every chamber contains a module of Drift Tubes plus one layer of RPCs for MB3 and MB4 and two layers of RPCs for MB1 and MB2.

A schematic layout of a DT chamber is shown in Fig. II.3. Each DT has 12 layers of contiguous drift tube cells. The layers are grouped in three "Superlayers" (SL), each one consisting of 4 staggered layers of DT cells. The innermost and outermost SLs, labeled SL1 and SL3 in the figure, are dedicated to the ϕ coordinate measurement in the CMS bending plane, while the central SL, labeled SL2, measures the z coordinate of a muon traversing the chamber in the r-z plane. The radial coordinate is measured using an extrapolation from the three superlayers.

The elements SL2 and SL3 are separated by a honeycomb spacer in order to give a better measurement resolution to the SL1 and SL3 combination. The outermost stations, named MB4, located outside the steel return yokes of the CMS magnet, have only two SLs measuring the hit position in the ϕ coordinates.

The individual Drift Tubes are actually cells made of aluminum to ensure good mechanical precision and stiffness. Each DT cell contains a stretched high voltage anode wire in the middle of the cell surrounded by a volume of gas. The layout of a DT cell is shown in Fig II.4. The distance

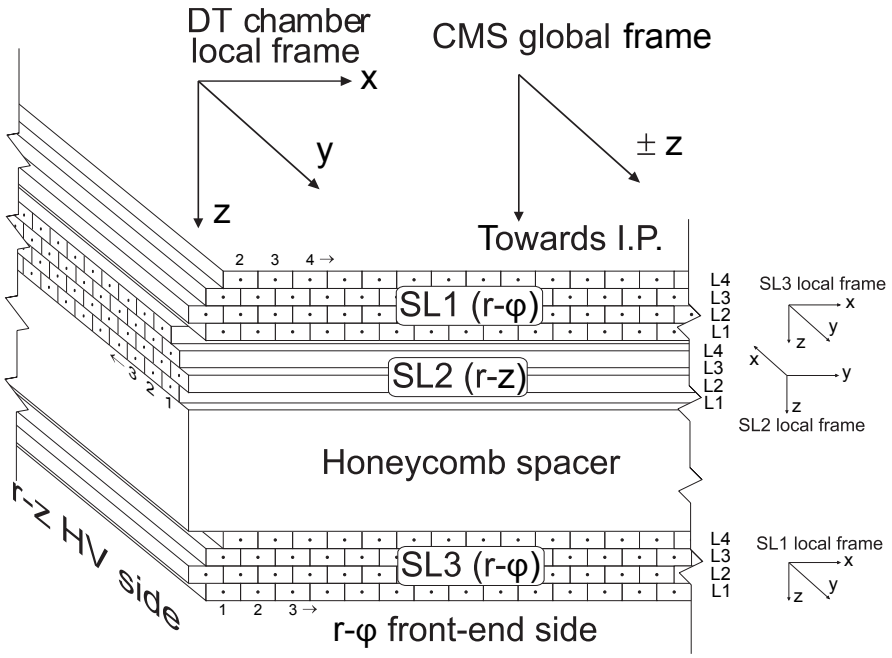

Fig. II.3. Schematic layout of a DT chamber. SL1 and SL3 are used to measure the ϕ coordinate, while SL2 measures the z coordinate along the direction parallel to the beam [12].

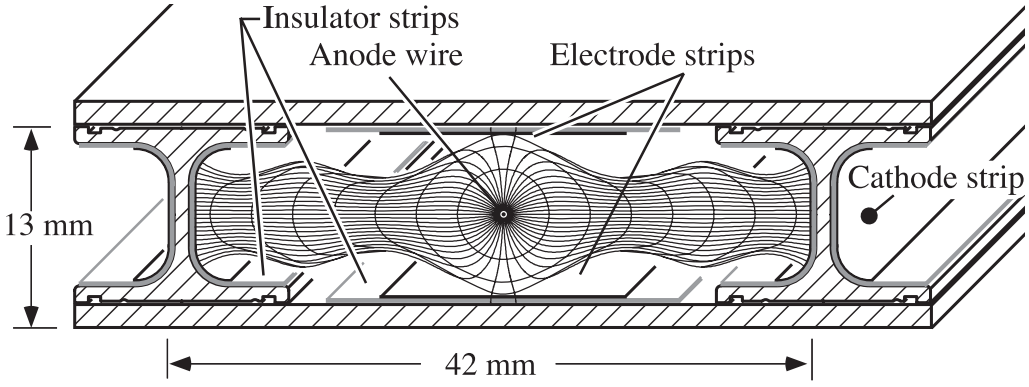

Fig. II.4. Layout of a DT cell, showing the electric field lines in the gas volume as well as the multiple components of each individual drift cell [12].

between the anode wires of consecutive DT cells is 4.2 cm. The cells are separated by 1 mm thick aluminum I-shaped support beams. The supports are glued between two 2.5 mm thick aluminum plates that separate consecutive layers. Aluminum strips, named "electrode strip" in the figure, are placed below and above the anode wire of the cell to shape the electric field lines. This electric field shape guarantees a good linearity of the cell behavior over almost the entire drift volume. The chambers are operated with an Ar/CO_2 (85/15) mixture. The voltages applied to the electrodes are 3600 V for wires, 1800 V for strips, and negative 1200 V for cathodes.

When a charged particle crosses a DT cell, it knocks out electrons from the gas that follow the electric field produced by the wire and create an avalanche of secondary ionization electrons. This creates "hits" in the adjacent cells that can be used to extrapolate the position of the muon and the bending angles of the trajectory, see Fig. II.5.

The electron drift velocity is about 54 μm/ns. The DT readout electronics is capable of recording multiple hits in the same cell, with a dead time of 150 ns between consecutive signals. At the operating value of the magnetic field equal to 3.8 T inside the solenoid, the magnetic field in the return yoke ranges between 1.2 T and 1.8 T. Inside the active volume of each DT chamber, the residual magnetic field is generally small (below 0.2 T) so we can ignore the magnetic bending inside the DT chambers. However, MB$\pm$2 stations, due to edge effects, have a radial magnetic gradient of significant magnitude [12].

Because there are two superlayers dedicated to measure the ϕ coordinate, a simple extrapolation between the hits in SL1 and SL3 can be used to reconstruct the local path that the muon traveled inside the DT chamber along with the bending angle measured with respect to the local normal. This bending angle ϕ_B depends only on the tangent approximation of curvature of the entire trajectory of the muon as it was bent by the magnetic field. Since the bending depends only on the transverse momentum, the bending angle measured at the station, ϕ_B, is dependent on the trans-

verse momentum of the particle p_T. Moreover, using the extrapolation from SL1 and SL3, it is also possible to precisely calculate the angular coordinate position ϕ of the hit with respect to the global coordinates of the barrel muon system. The information coming from the SL2 can be used to calculate the z position of the hit and a combination of the three superlayers can be used to extrapolate the radial position (r) of the hit.

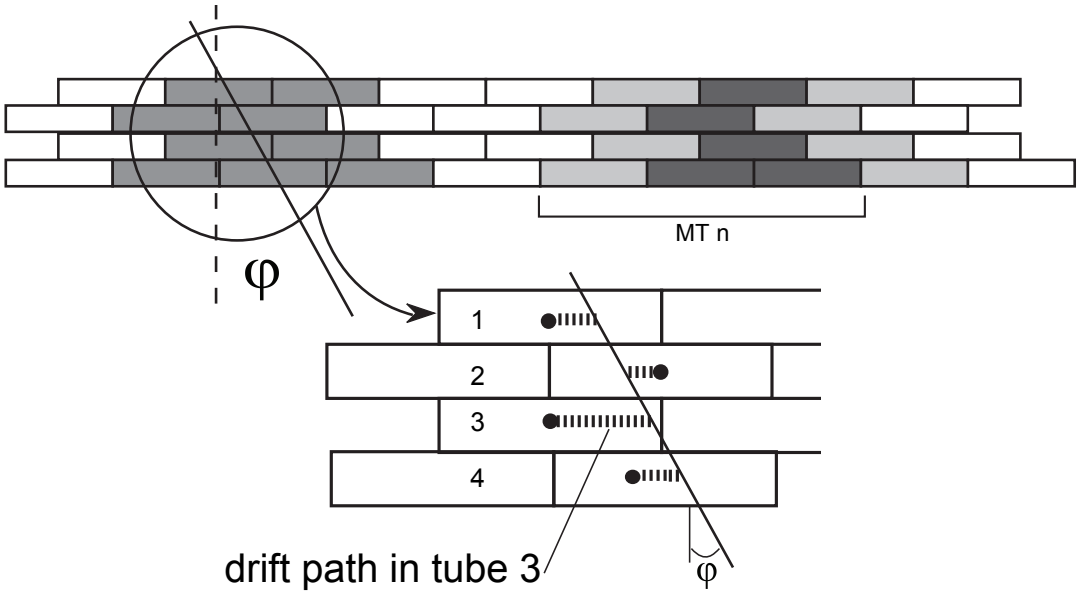

Fig. II.5. Drift Tubes basic function diagram. A muon creates electrons that are accelerated toward an anode wire inside each tube. By measuring times of the hit arrival (ionization avalanche arrival) we can reconstruct the path of the muon [16].

In the online trigger, the Track Finder uses local reconstructed stubs to build a track by matching segments and assigning a p_T value using the information from the bending of the track. The pairwise matcher extrapolates stubs from one station to another station and tries to find the closest nearby segment among many that might be present in each station at the given time. The algorithm also measures the angular position difference, value that will be later used to assign the p_T. Redundancy from the 4 stations is useful in case a muon misses any of these stations.

Once the pairs have been correlated, the track is assembled from the selected stubs and values of η and ϕ are assigned to this track with respect to the second muon station. Using the angular position difference a value for p_T can be assigned as well as a quality value from the local bending angle measured at each station.

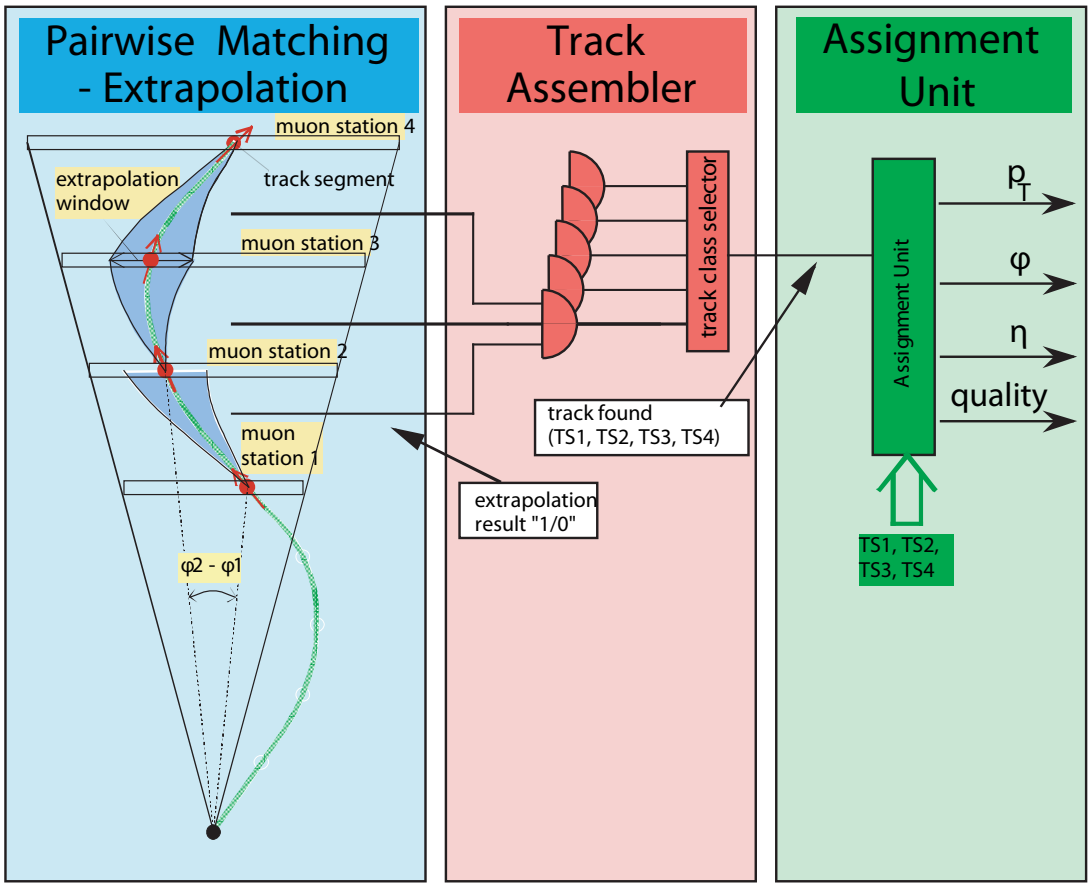

Fig. II.6. Illustration of the Track Finder algorithm up to the assignment of the kinematic and position variables p_T, η, ϕ and quality [12].

The values of the p_T and quality will be later used to further improve the background rejection of low momenta muons. Hence a mismeasurement of such quantities will result in the entire track, and henceforth the event, to be rejected.

II.3 Endcap Regions of the CMS experiment

The Muon detector system in Endcap regions (ME) is prone to high levels of background, expected from low momenta primary and secondary muons and charged particles in general that scatter off of the interaction point. For this reason, Cathode Strip Chambers (CSC) were chosen to cover the Endcap region instead of Drift Tubes (DT), as CSCs can deal with the increased amount of background in a better way. Moreover, the cathode strip technique of measuring position by the averaged center of charge deposition in strips works better in the presence of high momentum muon bremmstrahlung than DT.

The CSC chambers contain six layers of radial cathode strips to precisely measure the ϕ coordinate and six layers of nearly orthogonal anode wires whose signals are used to measure the non bending η coordinate. In the online, the CSC Local Trigger uses the six-layer redundancy of the CSC chambers to provide precise position information as well as to provide high rejection power against backgrounds. Muon segments, also known as Local Charged Tracks (LCTs) are found in the nearly orthogonal cathode and anode projections by somewhat different algorithms and by different electronic boards. For cathode and anode segments (CLCTs and ALCTs), the number of layers hit and the position and track angle through the chamber is reported. Up to two CLCTs and two ALCTs are found in each chamber during any bunch crossing. The two projections are then combined into 3 dimensional LCTs by timing coincidence. Each correlated LCT then provides to the CSC Track Finder a precision measurement of the bend coordinate (ϕ), bend coordinate angle of passage through the chamber (ϕ_b), approximate measurement of the non-bend angle coordinate (η), and identification of the muon bunch crossing (bx).

The most precise track measurement is obtained by charge digitization and precise interpolation of the cathode strip charges. For the online reconstruction in the trigger, a simpler and more robust method is used for the CSC system to achieve half-strip localization of the muon track in each cathode layer. This is done by a comparator board that compares the amplified and shaped signals

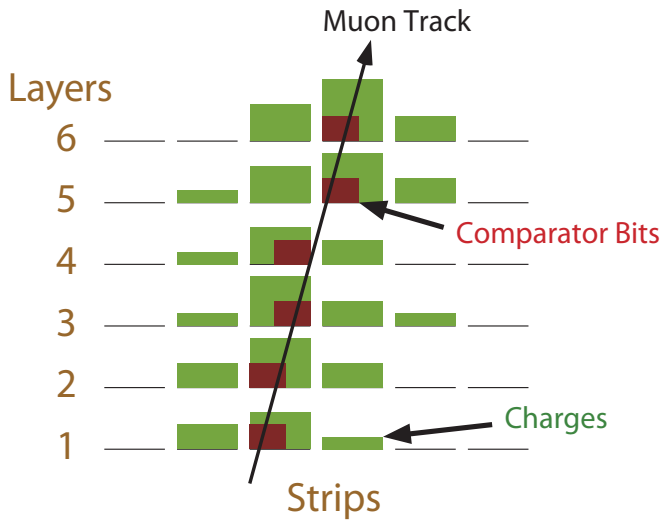

Fig. II.7. Cathode LCT formation using cathode comparator bits [12].

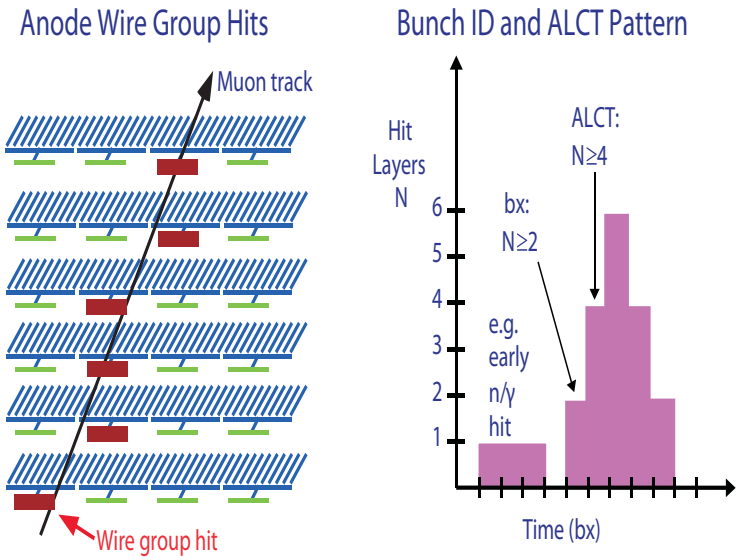

Fig. II.8. Anode LCT formation from wire group hits (left), and bunch crossing assignment based on numbers of hit layers (right) [12].

from adjacent strips. If a strip signal is found to be larger than those on its neighbors, a hit is assigned to the strip. Simultaneous comparison of left versus right neighbor strip signals allows assignment of the hit to the right or left side of the central strip, effectively halving the resolution. The six layers are then brought into coincidence in LCT pattern circuitry as shown in Fig. II.7. This establishes position of the muon to an RMS accuracy of 0.15 strip widths that range from 6 to 16 mm in width. Because of the slow 150 ns rise time of the cathode amplifier and shapers, the cathode electronics provides only a crude measurement of the bunch crossing.

In the CSC muon system, anode wires are spaced by about 3 mm. The anode wires are hard-wired together at the readout end in groups of 10-15 wires to reduce channel count. The algorithm used in determining muon segment position and bunch crossing in the anode view is shown in Fig. II.8. Anode signals are fed into the amplifier and constant fraction discriminators. Since the drift time can be longer than 50 ns, a multilayer coincidence technique in the anode LCT pattern circuitry is used to identify the bunch crossing. For each spatial pattern of anode hits, a low coincidence level, typically 2 layers, is used to establish timing, whereas a higher coincidence level, typically 4 layers, is used to establish the existence of a muon track and associate it with a certain bunch crossing by the shape of the pattern.

The stubs from all stations are sent to the Track Finder whose goal is to reconstruct tracks in the CSC endcap muon system and to measure the transverse momentum (p_T), pseudo-rapidity (η), and azimuths angle (ϕ) of each muon. Although this task is the same for the DT and CSC muon systems, the optimization of the design of the Track Finder is significantly different for each muon system because of the different logical partitioning of the trigger primitives and the non-axial magnetic field in the endcap region. The algorithms of the CSC Track Finder are inherently 3 dimensional to achieve maximum background rejection, as illustrated in Fig. II.9 and II.10. Moreover, the measurement of p_T uses spatial information from up to three stations to achieve a precision similar to that of the DT Track Finder despite the reduced magnetic bending in the endcap.

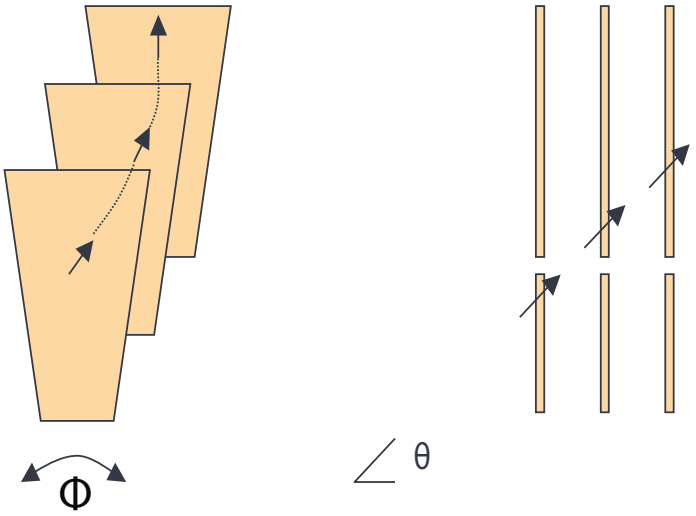

Fig. II.9. Illustration of the three-dimensional track finding procedure. In the ϕ view (left) and θ (or η) view (right) [12].

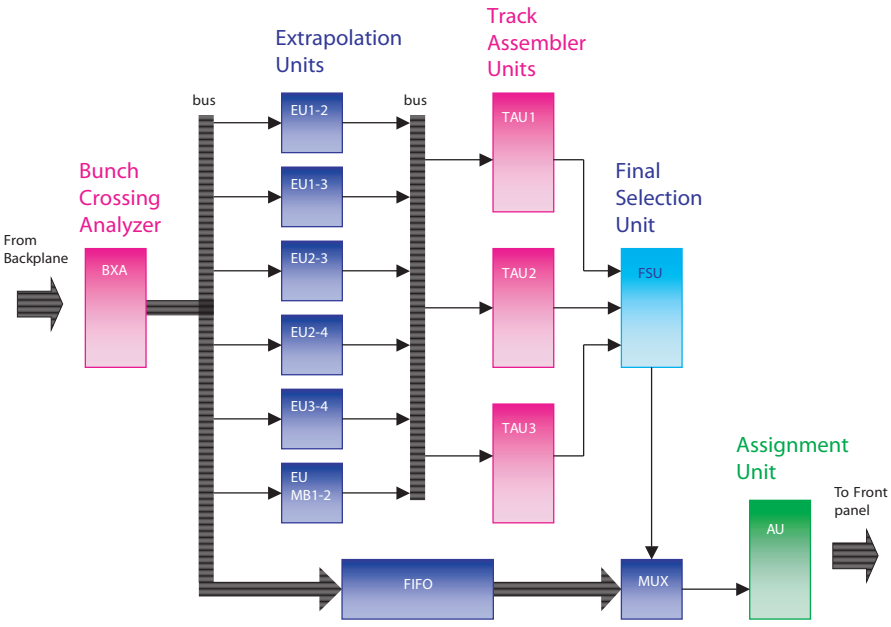

Fig. II.10. Illustration of the Track Finder algorithm, implemented in the Sector Processor [12].

II.4 CMS Muon Trigger System

The information generated by each collision is about 1-2 MB of raw data. At 40 MHz collision rate, the amount grows up to 73 TB of data being produced every second. For an experiment that runs for months collecting data, it will quickly surpass the capabilities of current supercomputers and even if we manage to store it all, the amount of data would be too large to analyze efficiently and within a reasonable amount of time. The CMS experiment uses a triggering system designed to perform ultra fast calculations to decide which collision events are going to be kept and which ones are going to be rejected. A clever trigger system can reject most of the non interesting events (background) while keeping the data we are interesting in observing (signal). The Muon Trigger is composed of two elements:

- The Level 1 Trigger, which identifies muons, determines their transverse momenta and locations and assigns the trigger data to the correct bunch crossing. Its ultimate goal is to decide whether to accept or reject an event and to generate the corresponding signals to be send to the second level of triggering.

- Muon High Level Trigger (HLT), which performs a much more detailed reconstruction of data events and sends its output of accepted events to the offline storage.

From the original 40 MHz rate of raw data, the L1 Trigger reduces it down to a few kHz. That is still a significant but manageable for the LHC computer farm amount of data. The Muon HLT further reduces the rate output of the L1 down to about 10 Hertz, at which point it can be safely stored offline for future studies.

Therefore, the goal of the Trigger system is to reduce as much background rate as possible while keeping as many potentially interesting events as possible.

Trigger selections include a minimum threshold for the transverse momenta of the detected muons and might require other objects such as electrons or jets. However, for the high luminosity HL-LHC regime, the current algorithms used for muon reconstruction at Level-1 have insufficient background rejection power to maintain acceptable efficiency for signal events.

A preliminary solution designed to keep the trigger rate within certain values and improve the overall reconstruction efficiency relies on the combination of the Muon and Track systems for Level-1 triggering.

The Tracker System consists of two main detectors: a silicon pixel detector, covering the region from 4 to 15 cm in radius, and 49 cm on either side of the collision point along the LHC beam axis, and a silicon strip detector, covering the region from 25 to 110 cm in radius, and within 280 cm on either side of the collision point along the LHC beam axis. The CMS silicon pixel detector has 66 million active elements and it's designed to provide the determination of three high precision three-dimensional points on track trajectories within a precision of 100 μm in the $r - z$ coordinate. The CMS silicon strip detector has 9.3 million active elements that deliver up to four $r - z$ measurements on a trajectory with a precision up to 80 μm. For the HL-LHC regime, CMS plans to install a new Tracker detector capable of online triggering as part of the Level-1 trigger.

Combining the Tracker with the Muon system, allows us to take advantage of the Tracker capabilities with its excellent momentum resolution with the non-muon background rejection capabilities of the Muon system. Fig. II.11 shows the reconstruction efficiency and the trigger rate reduction of the the Tracker - Muon system combination vs Standalone Muon system.

However, due to the constrains associated with the time available for making a trigger decision at Level-1, the Track Trigger system will be only able to efficiently reconstruct patterns corresponding to tracks that project back to the beamline. Therefore, muons originating from displaced vertices

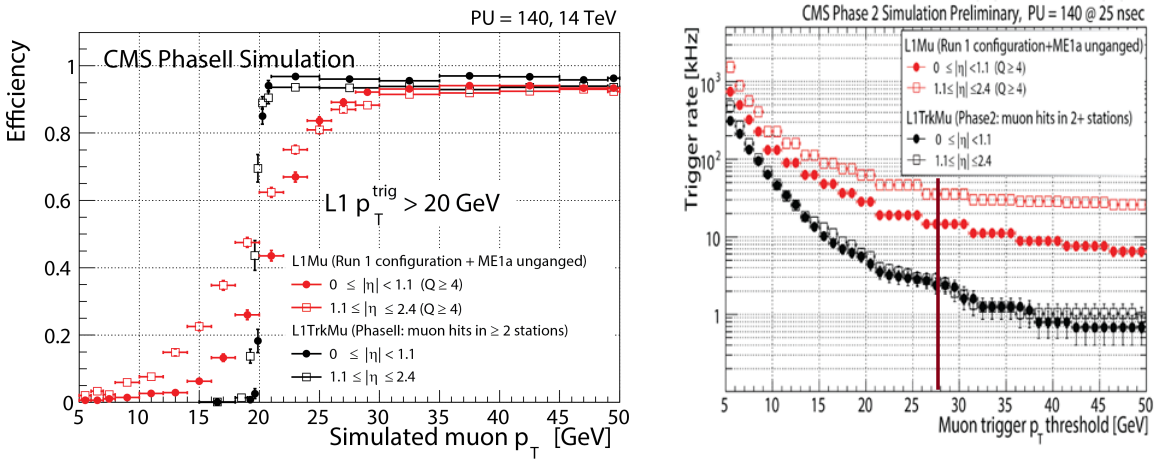

Fig. II.11. Improvements of the Muon-Tracker system (black) over the Standalone Muon System (red). The turn on efficiency curves are improved (left) while the trigger rates are kept low (right).

and not pointing back to the beamline will not be reconstructed by the Track Trigger. Hence, an efficient algorithm for detecting displaced muons has to be primarily based on standalone muon reconstruction information. Successful implementation of such algorithm would however require an improved background rejection.

Since displaced muons might come from energetic mother particles that could hold keys for new physics, it's imperative for the CMS to be able to reconstruct such muons. In the next chapter we will discuss the limitations of the current standalone muon trigger in more detail.

CHAPTER III

LIMITATIONS OF THE CURRENT MUON L1 ALGORITHM

III.1 Current Muon L1 Algorithm

Muons are produced in a proton - proton collision. However, a number of well motivated models of new physics predict signatures, in which muons are produced in decays of new particles that can travel a significant distance from the primary production point before their decay to muons. These *displaced muons* will not point back to the interaction point and the existing algorithms are unable to reconstruct them.

We use the track impact parameter, d_{xy}, to asses the displacement of the non prompt muons. The impact parameter is defined as a distance between the interaction point and the point of closest approach of the track to the interaction point. The secondary vertex is the position at which the muons (or any other secondary particles) are produced. Fig. III.1 shows the definition of this variable.

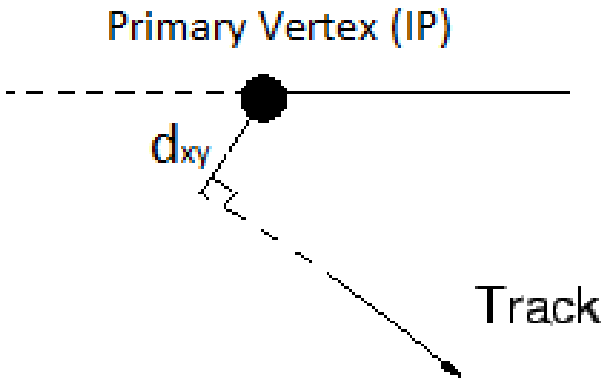

Fig. III.1. The impact parameter, defined as the closest point of approach to the interaction point, is the figure of merit used to measure the degree of displacement.

We created a simulated sample of events using Pythia event generator [17] for the process:

$$pp \rightarrow \ H \ \rightarrow \ Z_D Z_D \ \rightarrow \ \mu^+\mu^-\mu^+\mu^- \tag{III.1}$$

In this process, a proton - proton collision generates a Higgs boson that decays into two so called "Dark Z-bosons" that are part of a new hidden (or dark) sector which only weakly interacts with the ordinary particles. We simulate the creation of heavy Dark Z with lifetime long enough for them to travel a distance, $c\tau$, of 1000 mm, which decay into pair of muons in a secondary vertex. The mass of the Dark Z was fixed to be 20 GeV. Fig. III.2 shows the distribution of the impact parameter for these model parameter choices, emulating about 80, 000 collision events.

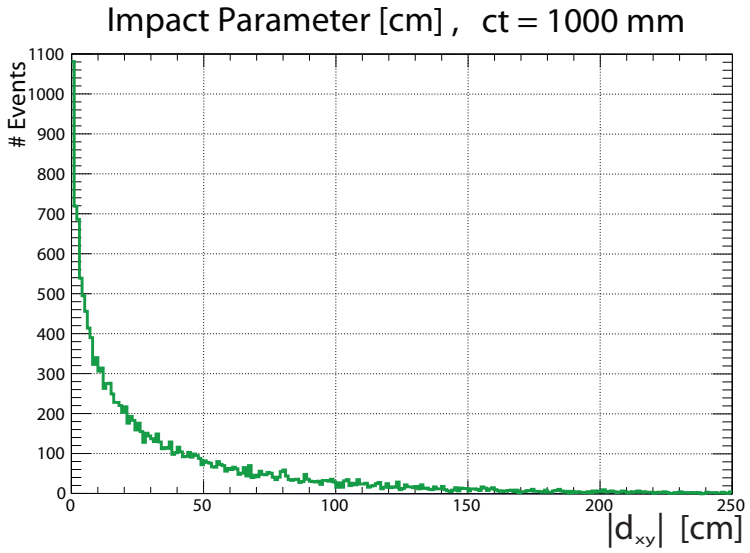

Fig. III.2. Distribution of the impact parameter for a massive particle with average lifetime of cτ 1000 mm.

As Fig. III.2 shows, for this particular scenario, we can find particles with impact parameter as big as 200 cm. However, studies have shown that existing algorithms are not efficient for triggering on displaced muons. Fig. III.3 shows the reconstruction efficiency for a trigger that uses only the muon system (L1Mu) and a trigger that combines muon and tracker information (L1TkMu).

The efficiency for L1 Tracker Trigger quickly drops to zero as the impact parameter exceeds just a couple of millimeters. Note that the Standalone L1 muon trigger is still able to reconstruct such muons with large impact parameter, as illustrated in the same plot.

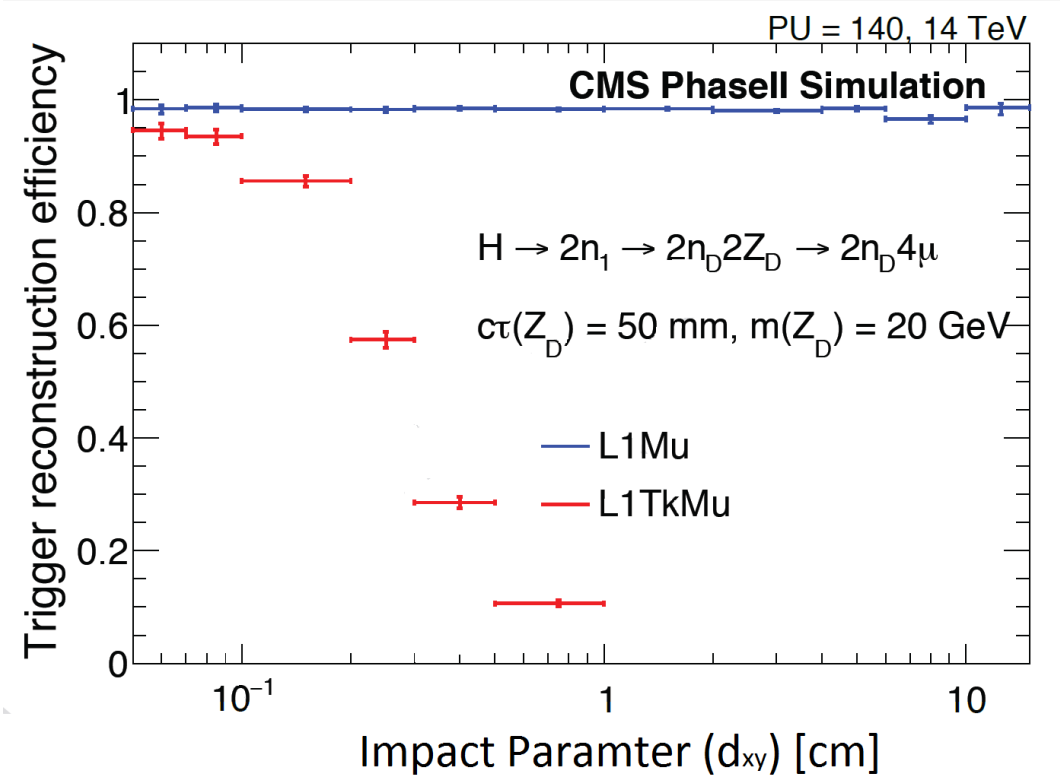

Fig. III.3. Efficiency of the existing algorithms on reconstructing displaced muons as a function of the impact parameter (d_{xy})for Standalone (blue curve) and combined Track + Muon (red curve) triggers.

However, while the L1 Muon Standalone Trigger is capable of reconstructing displaced muons, it significantly underestimates their momentum. Fig. III.4 shows the efficiency of the requirement that the reconstructed by the trigger transverse momentum of the muon candidate exceeds 20 GeV as a function of the true p_T of the muon. A large portion of the muons will have a significant displacement (as shown in Fig. III.2 and will therefore be discarded by the current algorithm.

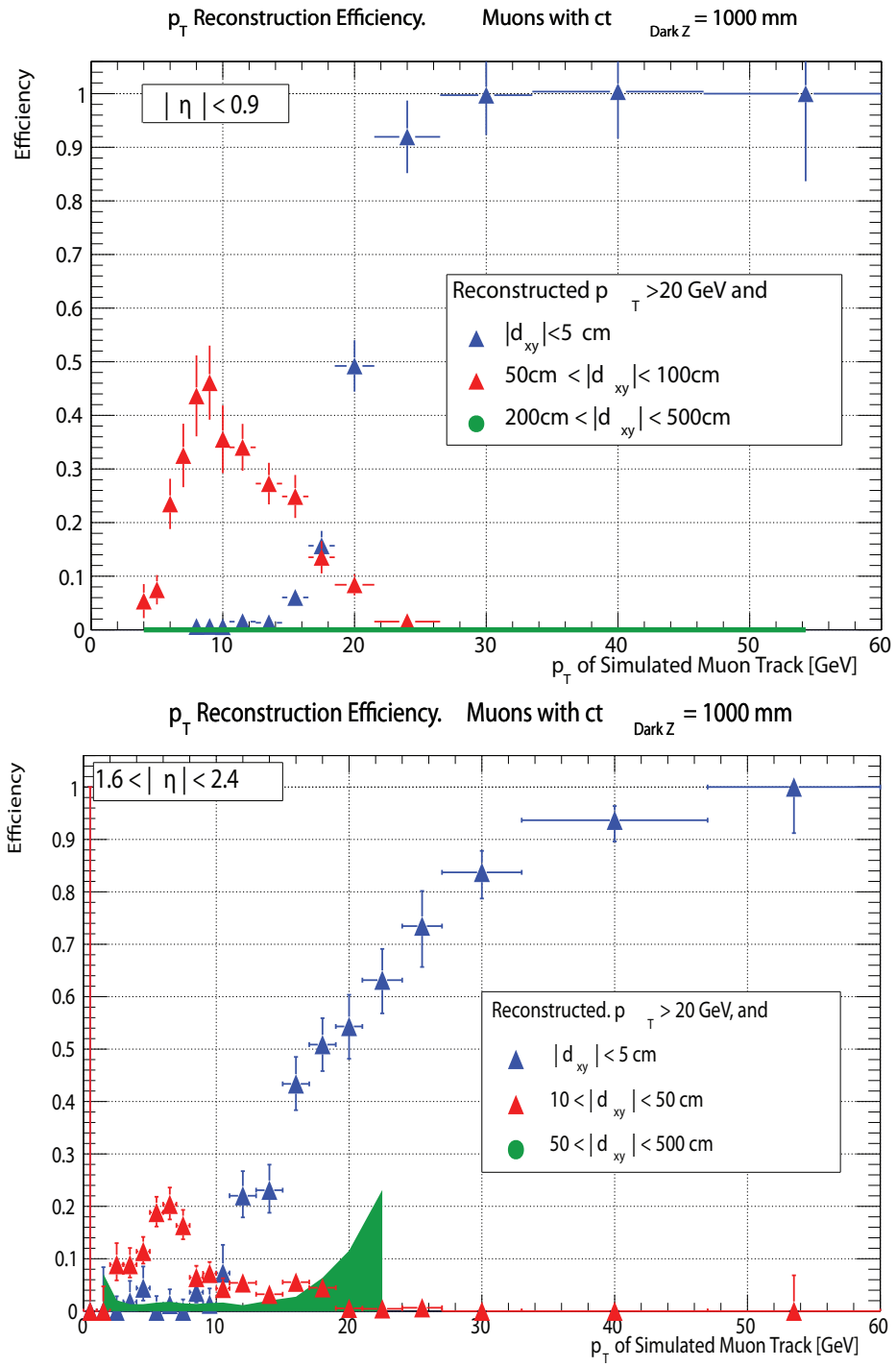

Fig. III.4. Efficiency of the requirement that the transverse momentum, reconstructed by L1 Standalone Muon trigger algorithm exceeds 20 GeV as a function of the true transverse momentum of the muon. Different curves correspond to different ranges of the impact parameter of the muons. Barrel Region (top) and Endcap Region (bottom).

III.2 Barrel Region Mismeasurement

The Level 1 Muon Trigger algorithm for the Barrel Region relies on the precise measurement of the ϕ coordinate in different DT stations. The almost uniform magnetic field inside the barrel region makes the relationship between the bending, which is measured by the difference in ϕ position between different Muon Barrel stations, to be directly related to the transverse momentum of the particle. Fig. III.5 illustrates pT assignment algorithm used by the DT standalone muon trigger for both prompt and displaced muons.

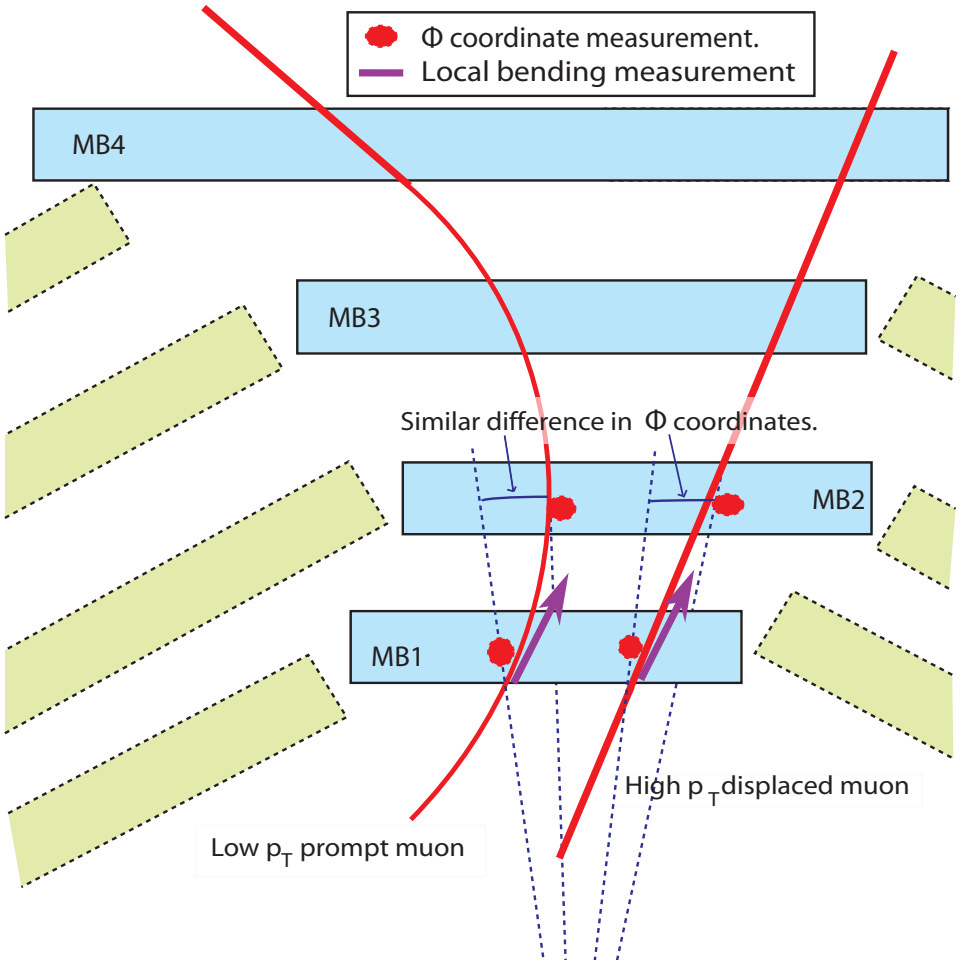

Fig. III.5. Displaced muons might have large difference on ϕ position, similar to prompt, low p_T muon. Mismeasurement on the p_T will cause the event to be rejected once a minimum p_T threshold is applied.

The relationship between the ϕ difference and the transverse momentum holds really well for prompt muons. Fig. III.6 shows that there is a inverse relationship that gives a narrow correlation of the ϕ difference variable with respect to the p_T. Therefore, if we measure the difference between stations MB1 and MB2, we can use a simple formula to estimate the transverse momenta of a prompt muon.

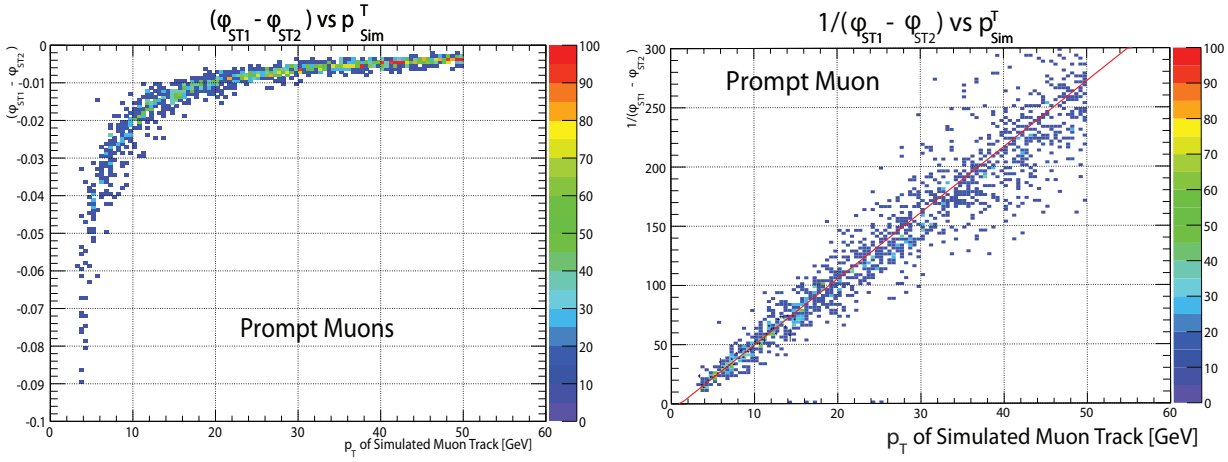

Fig. III.6. Difference in ϕ positions, $\Delta\phi$, measured in stations MB1 and MB2 vs traverse momentum, p_T for prompt muons (left). $1/|\Delta\phi|$ vs p_T forming a lineal relationship for prompt muons (right).

The relationship is simple enough that we can pre-calculate parameters to convert from $\Delta\phi$ to p_T. These pre-calculated values can then be stored in the form of a look up table (LUT) and can be implemented in electronics.

The redundancy of the CMS experiment allows us to reconstruct the p_T even if muon signals in any or both MB1 and MB2 chambers are missed. However, other combinations do not generate such simple and monotonous relationship with the p_T. Fig. III.7 shows the relationship between $\Delta\phi$ position measured in different MB stations vs the p_T of a prompt muon. It is still possible to compute the p_T in other stations if we split the non-monotonous relationship into low p_T and high

p_T regions, each holding a simple linear relationship.

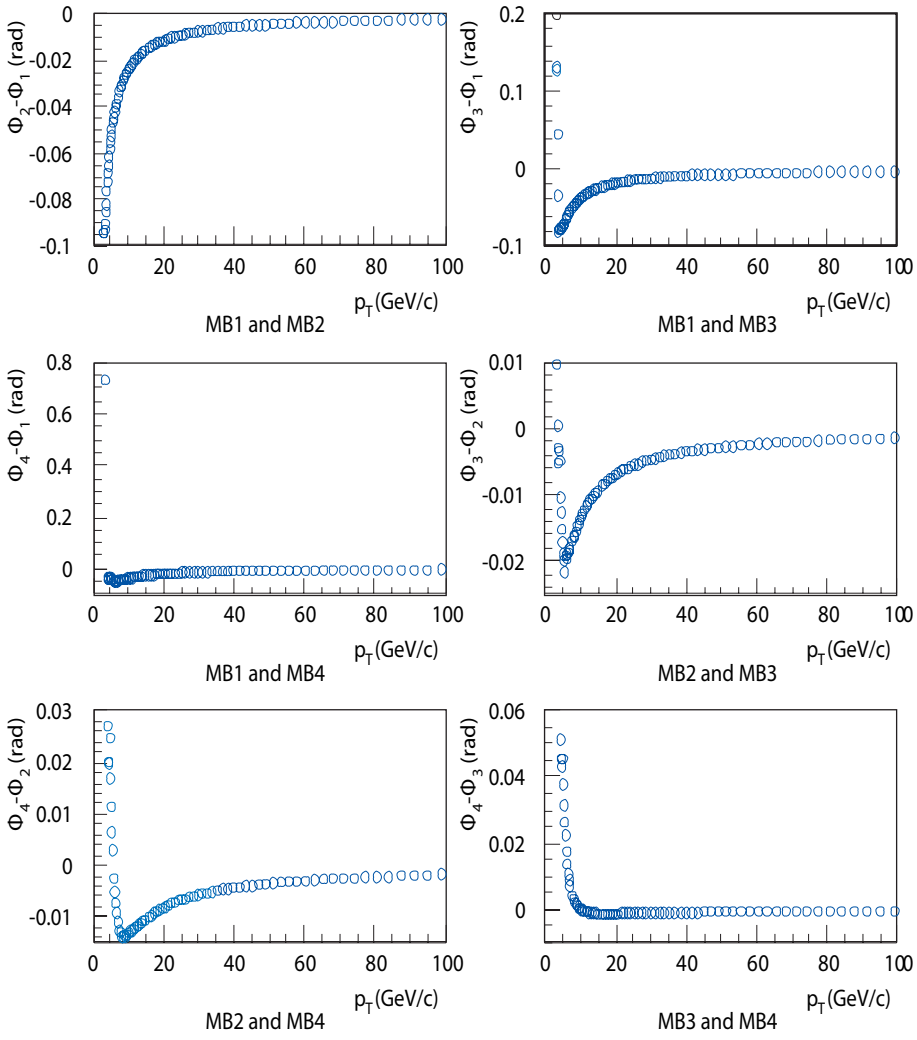

Fig. III.7. Difference in ϕ position vs p_T for all the possible combinations between stations in the Barrel Region. The non monotonous relationships are solved by splitting the tendency into low p_T and high p_T LUT [12].

In order to properly decide which LUT will be used, the algorithm measures the DT local bending in station MB1 (or MB2 if MB1 is missed). Assuming that a muon comes from the interaction point, a large DT local bending angle implies a large curvature and therefore a small transverse

momenta. Fig. III.5 shows the local bending angle measurement in the first station.

However, since displaced muon will have a inherently large bending angle, the L1 algorithm will chose to use the low p_T LUT to reconstruct them. Fig. III.8 illustrates how a high p_T displaced muon with large bending angle is reconstructed as a low p_T prompt muon.

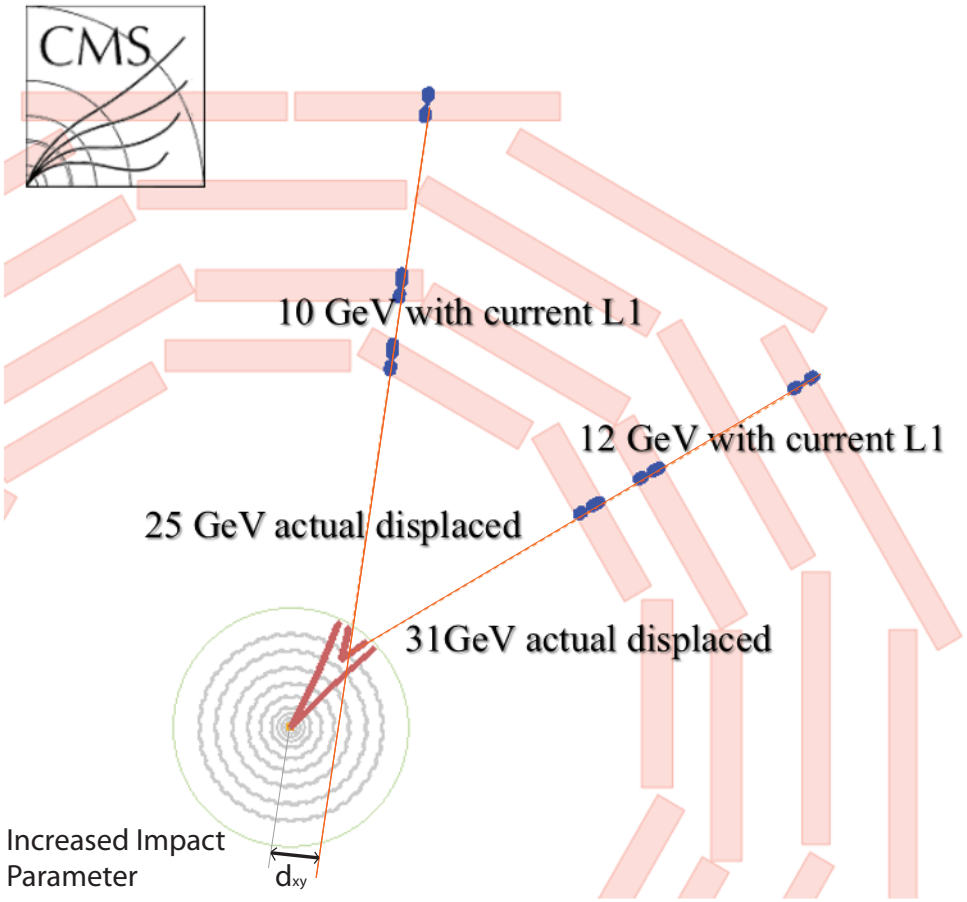

Fig. III.8. Displaced muon has a large bending angle at the first station. The current L1 algorithm uses the incorrect LUT to reconstruct it. Moreover, since displaced muons have path that resemble low p_T prompt muons, current L1 fails to reconstruct them properly. Events with displaced muons are likely to be rejected and its information lost forever.

However, the nice correlation between the measured $\Delta\phi$ and p_T observed for prompt muons is no longer there for displaced muons. A relationship between the difference in ϕ positions and p_T becoming dependent on the impact parameter, makes it unsuitable for reconstructing displaced muons as no prior knowledge of the displacement is available. Fig. III.9 shows that displaced muons don't have a nice relationship between $\Delta\phi$ and p_T that has been observed for prompt muons as illustrated in Fig. III.6.

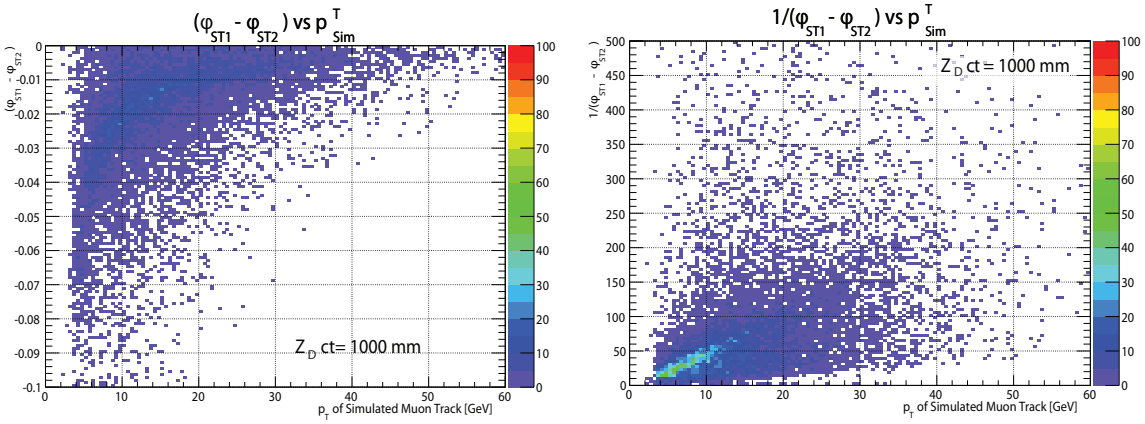

Fig. III.9. Difference in ϕ positions measured in stations MB1 and MB2 vs traverse momentum, p_T for displaced muons with $c\tau$ = 1000 mm (left). $1/\Delta\phi$ vs p_T is shown on right. No simple relationship can be drawn from these variables.

The result is that the current L1 Muon Trigger will likely assign a low p_T value to high p_T displaced muons. Once a sufficiently high trigger threshold is applied in order to keep the rates within limits of operation, events containing displaced muons whose reconstructed momenta has been severely underestimated by the trigger will be rejected.

Trigger selection efficiency with any reasonable value of the threshold will quickly deteriorate as the muon's impact parameter increases. Fig. III.4 clearly demonstrated the problem.

III.3 Endcap Region Mismeasurement

The L1 Trigger for the Endcap Region relies on the precise measurement of the ϕ coordinate by the CSC chambers in multiple stations. As in the barrel, the magnetic field will bend the charged particles and the difference in ϕ coordinate measured between different CSC stations can be related to this bending and therefore for the transverse momentum of the passing-by particle. Fig. III.10 illustrates the current algorithm.

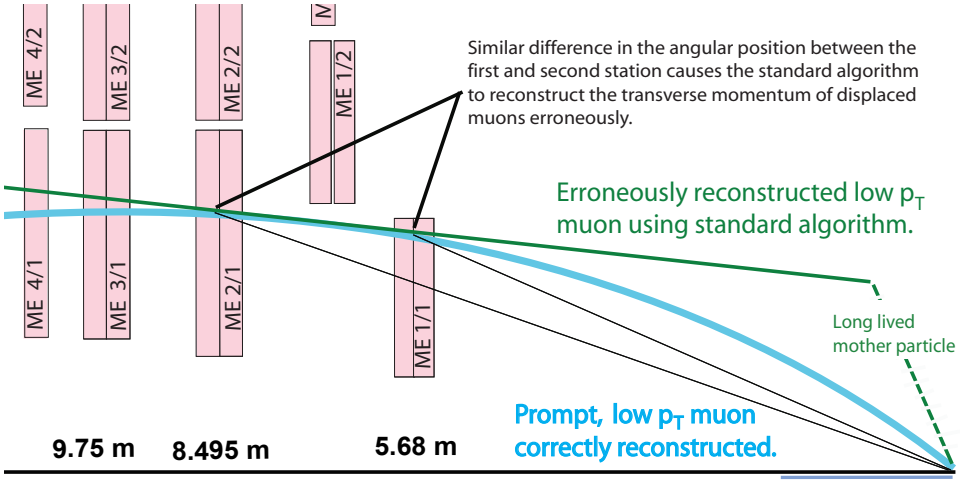

Fig. III.10. Current L1 Muon Trigger implementation relies on measuring the ϕ coordinate in different Muon Endcap stations. Displaced muons might have large ϕ differences similar to prompt, low p_T muon, causing them to be erroneously reconstructed as low p_T muons. Note, that bending of the prompt low p_T muon trajectory actually occurs in the plane transverse to the beam line and not in the longitudinal plane as shown in this drawing. We chose to present it this way to help readers get an intuitive feeling of the procedure used to measure muon momentum.

Since low p_T particles will bend more than high p_T particles, there is a theoretical inverse relationship between the transverse momenta and the amount of bending of the muon trajectory. We measure the amount of bending by comparing the ϕ coordinate change among Muon Endcap (ME) stations. The redundancy of the muon system allows for a particle to miss up to two stations and still be reconstructed properly, although the precision of the momentum measurement is reduced

if too few points are available of the momentum estimation.

There is a strong correlation between the ϕ difference and the transverse momentum for prompt muons. Fig. III.11 shows that there is a inverse relationship that allows estimating muon p_T by measuring the difference in position ϕ between station ME1 and ME2.

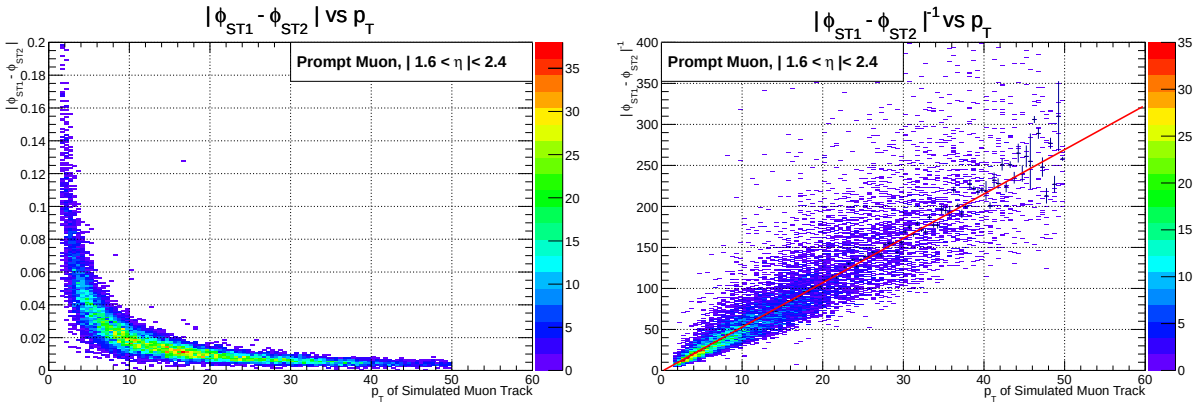

Fig. III.11. Difference in ϕ position measured in stations ME1 and ME2 vs transverse momentum, p_T for prompt muons (left). A nice inverse relationship can be drawn from these variables (right).

However, as it was the case in the barrel region, the difference in ϕ becomes dependent on the impact parameter. Fig. III.12 shows such dependence.

Since we can't measure the impact parameter at the L1 Muon Trigger, we can't construct a relationship between $\Delta\phi$ position, p_T and d_{xy} that will properly reconstruct both prompt and displaced muons. Fig. III.13 shows that there is not a simple relationship between $\Delta\phi$ position and p_T for displaced muons with cτ = 1000 mm.

Once any reasonable threshold on p_T is applied, hypothetical signal events with displaced muons will be rejected by the trigger.

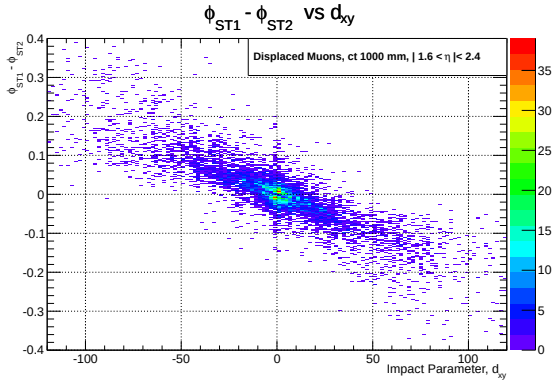

Fig. III.12. Difference in ϕ position measured in stations ME1 and ME2 vs impact parameter.

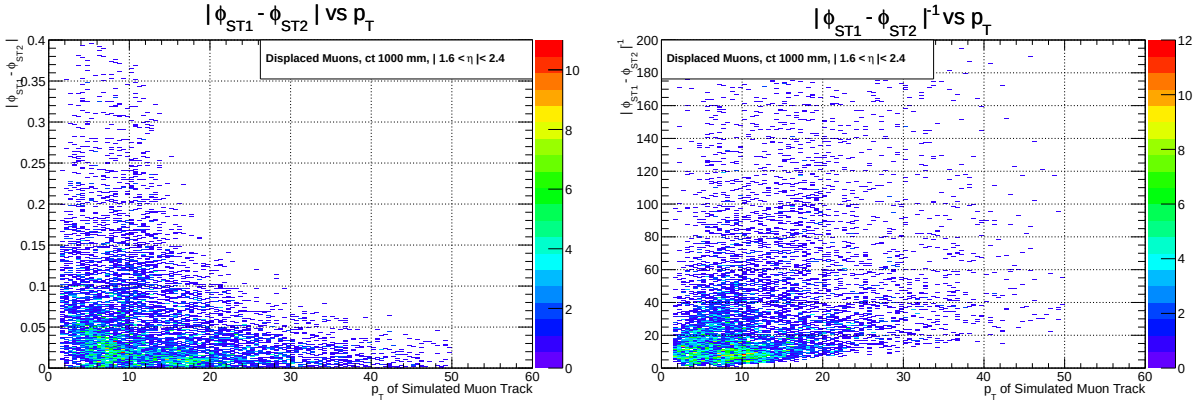

Fig. III.13. Difference in ϕ positions measured in stations ME1 and ME2 vs transverse momentum, p_T for displaced muons (left). $1/\Delta\phi$ vs p_T is shown on right. No relationship can be drawn from these variables.

In the next chapter, we propose an algorithm that works for reconstructing both displaced and prompt muons. We also identify a mechanism to maintain the trigger rate of such proposed trigger within reasonable bounds.

CHAPTER IV

STUB ALIGNMENT ALGORITHM AND RESULTS

The current algorithm relies on the difference in the ϕ coordinate to reconstruct the transverse momentum. However, as it was shown in the previous section, this variable $\Delta\phi$ cannot reconstruct the momentum for non-prompt muons.

In this chapter, we propose an algorithm and discuss the definitions of the variables, which are used to reconstruct the p_T of displaced and prompt muons.

IV.1 Stub Alignment Algorithm for the Barrel Region

From the basic principles, a muon with high p_T will travel in an almost straight line regardless of its impact parameter. If a muon is not prompt, the absolute bending angles measured at each station may be significant, but the variations in the local bending angles measured at different stations of the muon system should remain small. Using this property, we can define the difference in local bending angles measured at different stations, $\Delta\phi_B$ as the new variable to reconstruct the p_T of the muon.

Fig. IV.1 illustrates the basic principle of the algorithm. Even if the trajectory of a high p_T displaced muon resembles that of a low p_T prompt muon in the first two stations, the direction of the stubs at different stations will not differ considerably. We expect that a high p_T muons will leave stubs in the muon stations that will be pointing in almost the same direction and aligned in a straight line.

Low p_T muons will have stubs pointing at different directions that will depend on the radius of the curvature of its path, and therefore on the transverse momenta of the muon. Since this method

doesn't assume a muon coming from the interaction point, $\Delta\phi_B$, will be independent on d_{xy}.

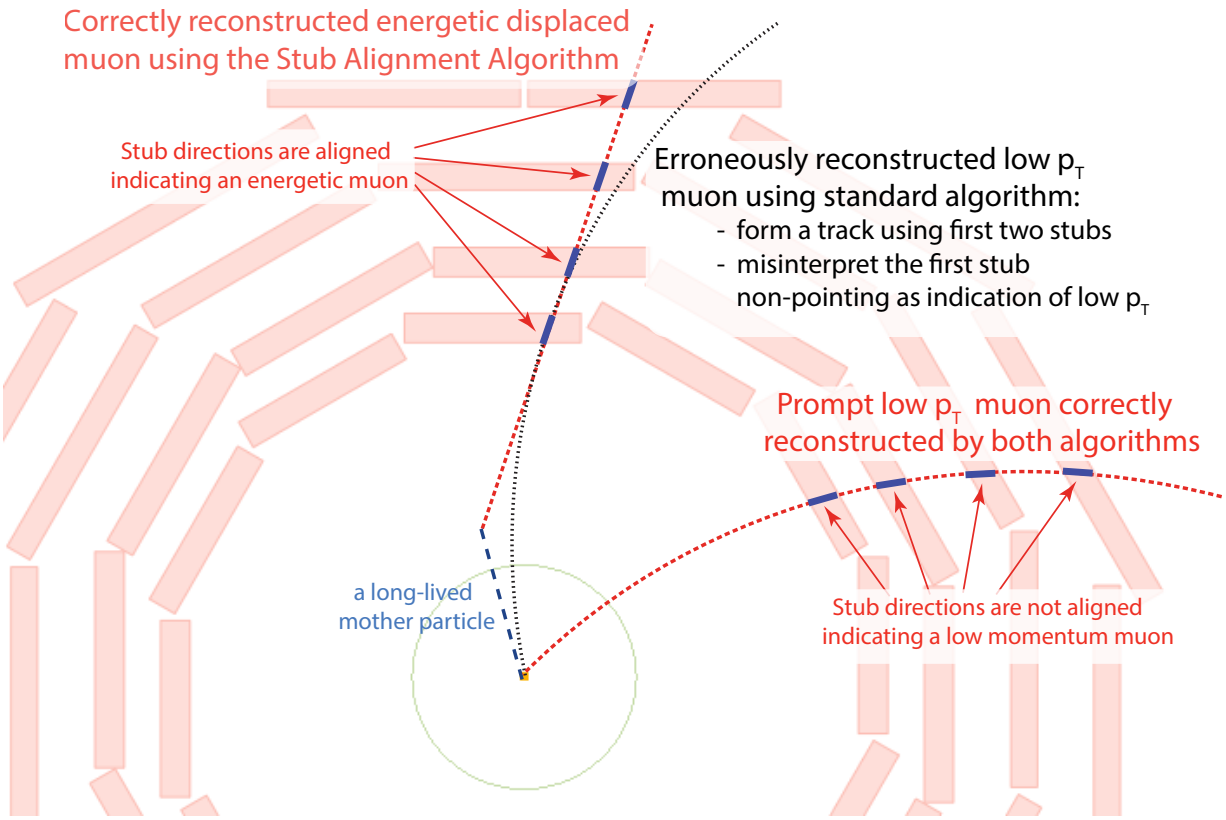

Fig. IV.1. High p_T displaced muon travels along (almost) straight line and leaves aligned track segments in the muon stations.

Fig. IV.2 shows the definition of this new variable in the Barrel Region where we use the direction of the stub instead of their position to create a variable, $\Delta\phi_B$ that relates to the p_T. Fig. IV.2 only shows $\Delta\phi_B$ measured between stations MB1 and MB4 but all other combinations are also possible.

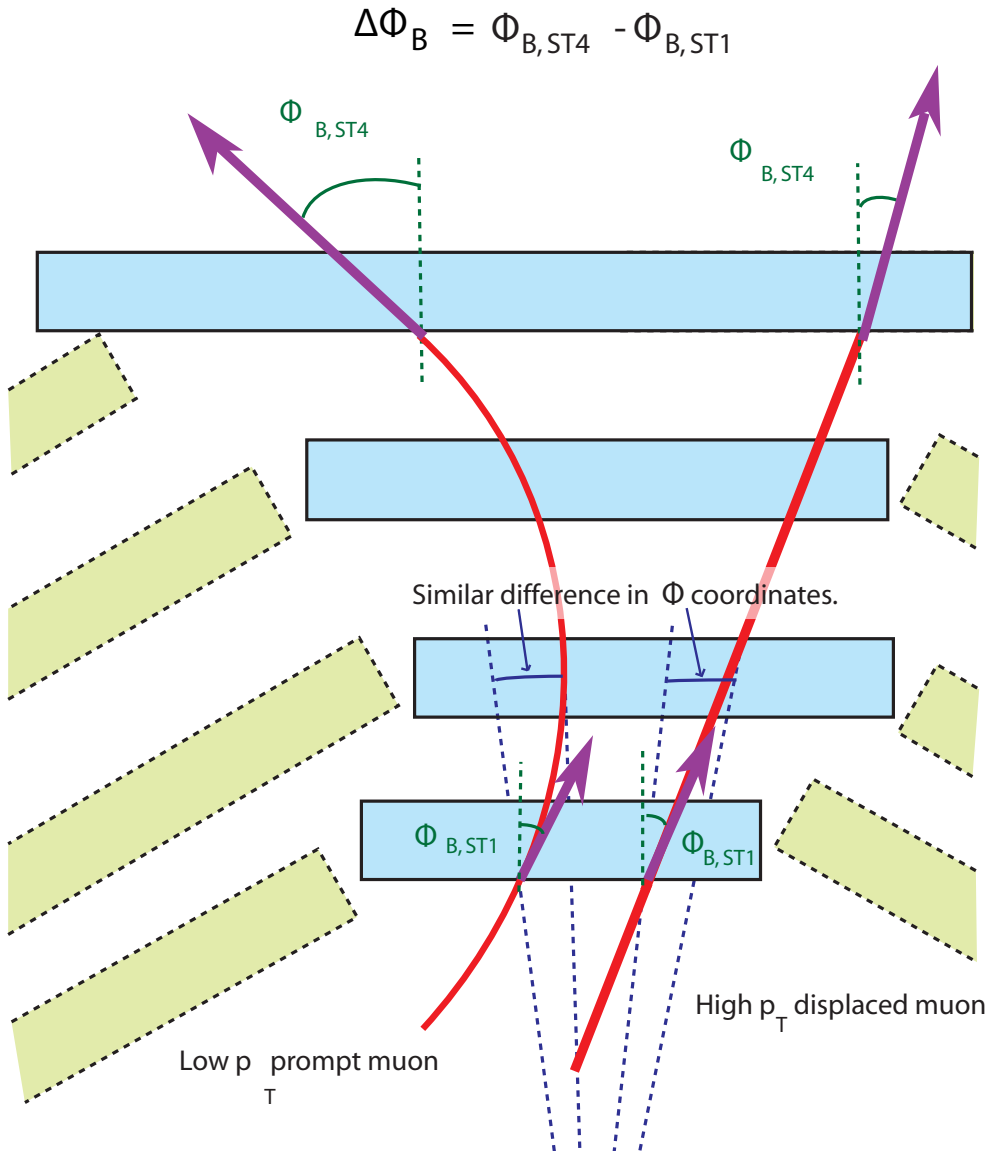

Fig. IV.2. Illustration of the proposed algorithm definition for the bending angle difference $\Delta\phi_B$ between stations.

Using the variable $\Delta\phi_B$ defined in Fig. IV.2, we can measure the correlation between ϕ_B and the muon p_T, taking into account all Muon Barrel chamber combinations. Fig. IV.3 shows the result, where we observe a good linear inverse relationship.

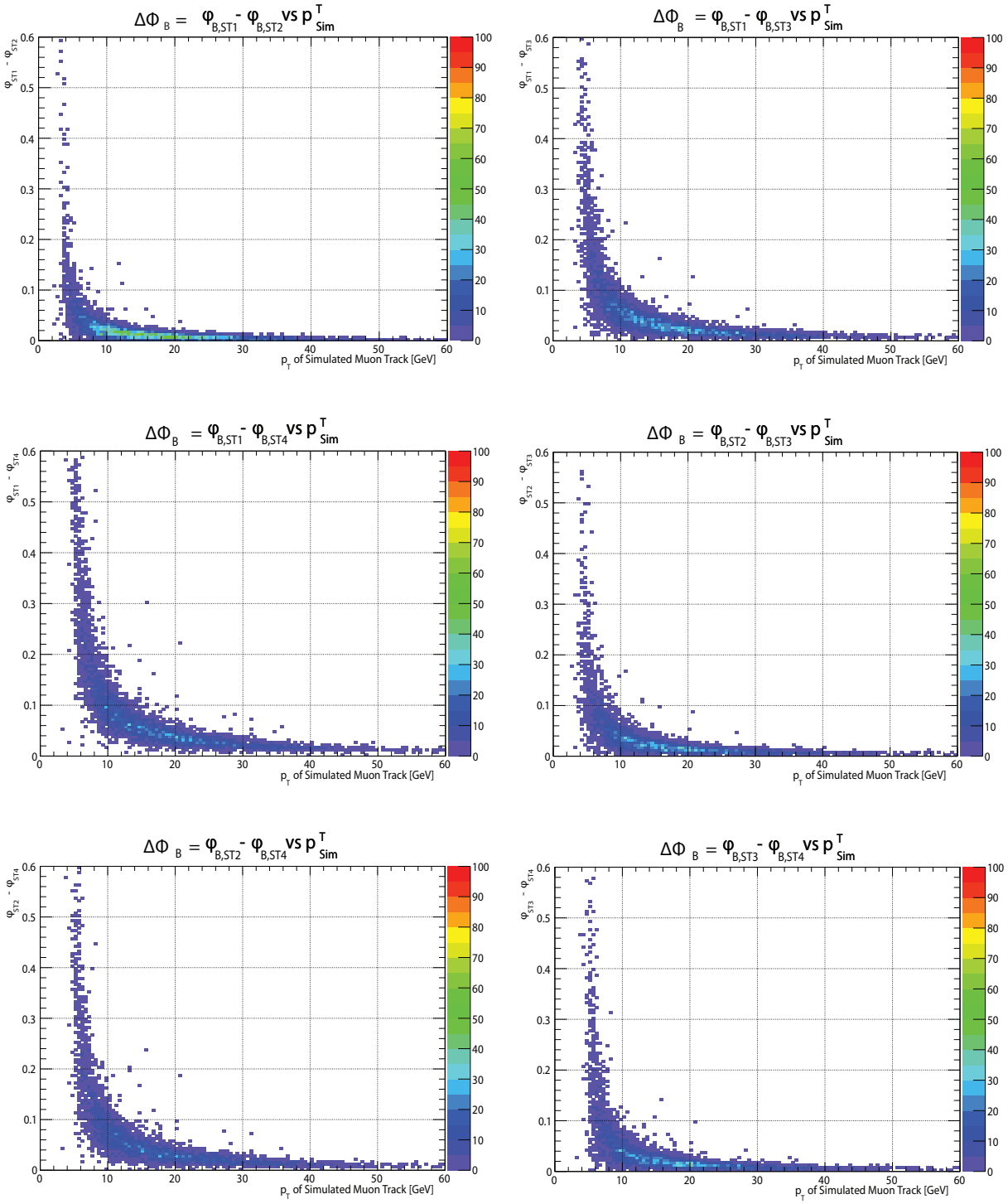

Fig. IV.3. $\Delta\phi_B$ measured at different stations vs p_T for displaced muons with cτ of 1000 mm, showing a clear inverse correlation between the variables. Compare to Fig. III.7.

Fig. IV.4 shows the correlation between $1/\Delta\phi_B$ and p_T, which can be used to assign the transverse momenta to displaced muons candidates.

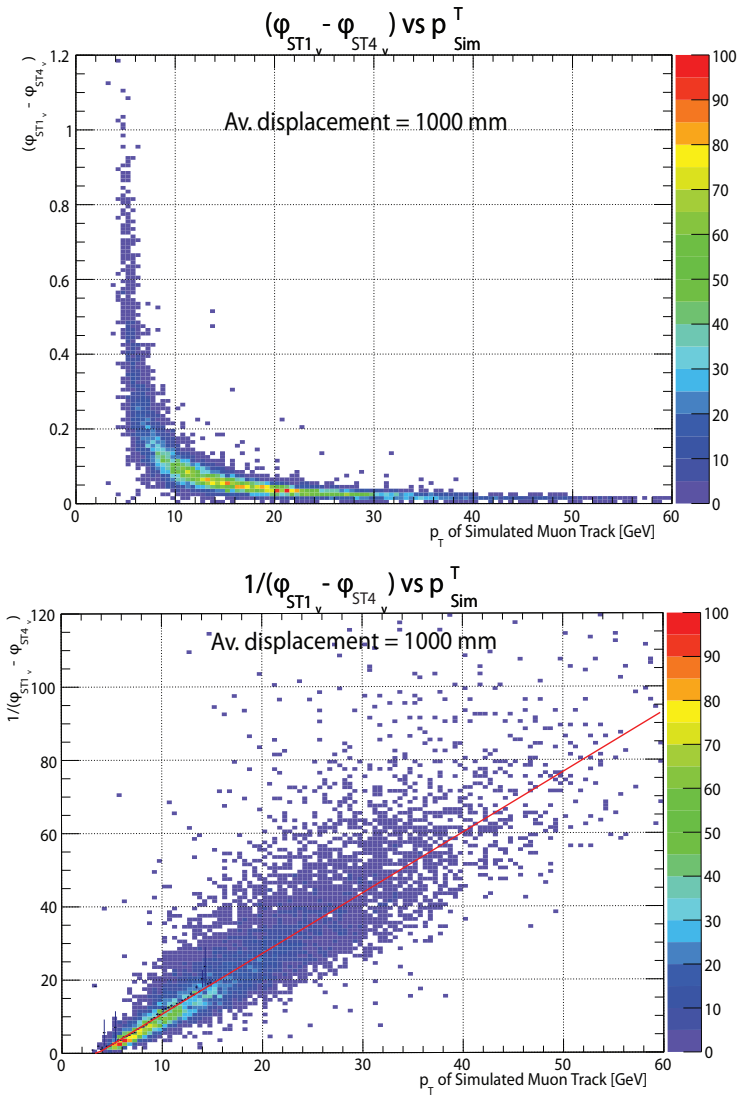

Fig. IV.4. Relationship between $\Delta\phi_B$ and p_T (top) clearly showing an inverse dependence (bottom).

Using Fig. IV.4 we can reconstruct the p_T from displaced muons using a simple linear formula. The results are shown in Fig. IV.5.

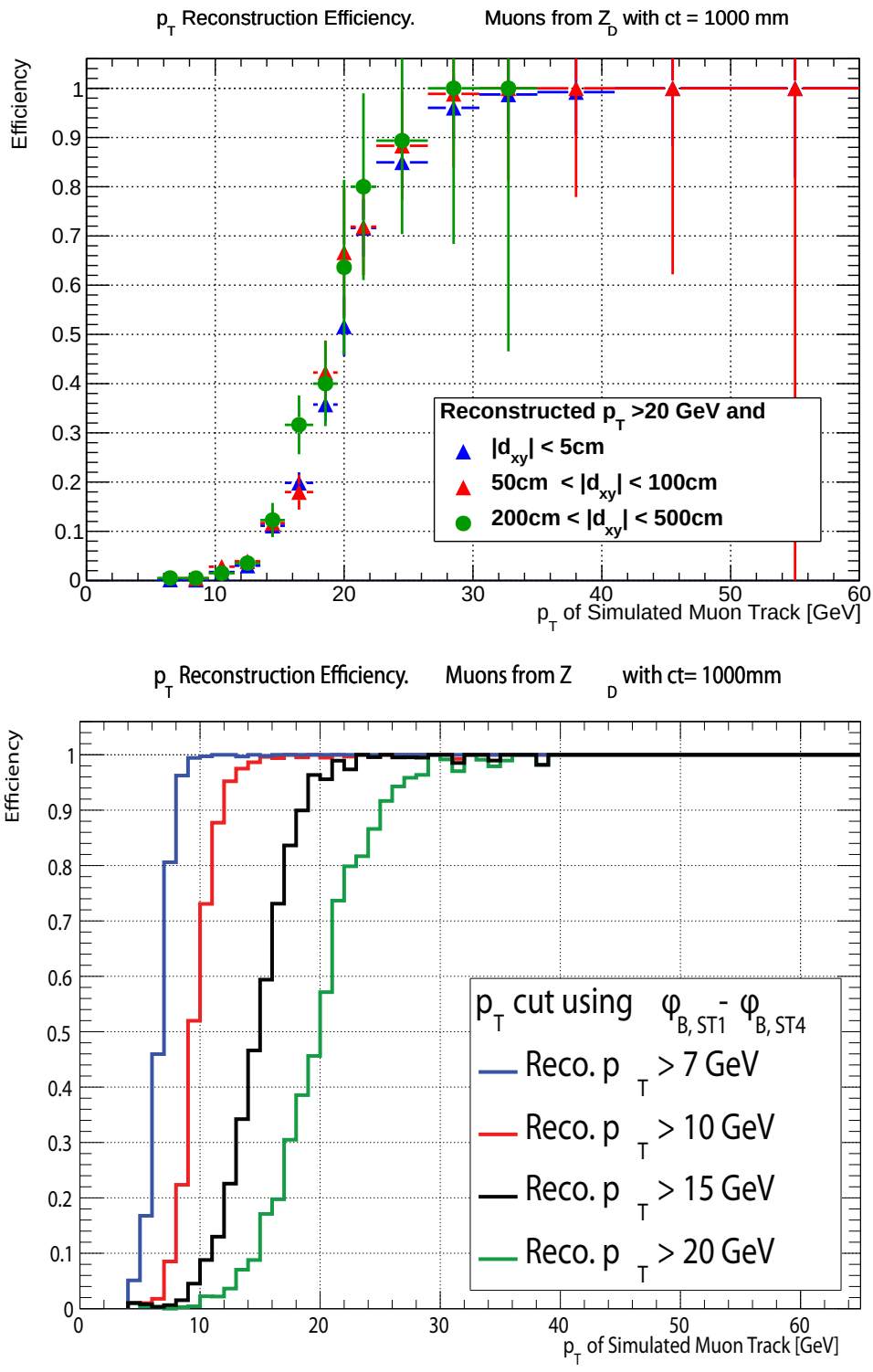

Fig. IV.5. Reconstruction Efficiency for the proposed algorithm reconstructing transverse momenta is independent of the muon impact parameter (top). Turn on curves using this algorithm (bottom). Both plots using a sample of simulated muons with ct 1000 mm.

IV.2 Position Alignment Algorithm for the Endcap Region

We can apply the same reasoning to the Endcap region and define a variable that relates the difference in local bending angle to the transverse momentum. However, the angular resolution of the CSC chambers used in the Endcap region is relatively poor. Therefore, we opted to combine features of the stub alignment algorithm with the p_T assignment based on stub positions.

By the first principles, we can construct a straight line from two points in the ME stations. By extrapolating the position to a third station we can have a rough idea where an infinitely high p_T muon will hit. The difference from the actual position to the extrapolated position in the third station will therefore be related to the p_T of the muon. Fig. IV.6 shows the basic definition for this $\Delta\Delta Y$ variable.

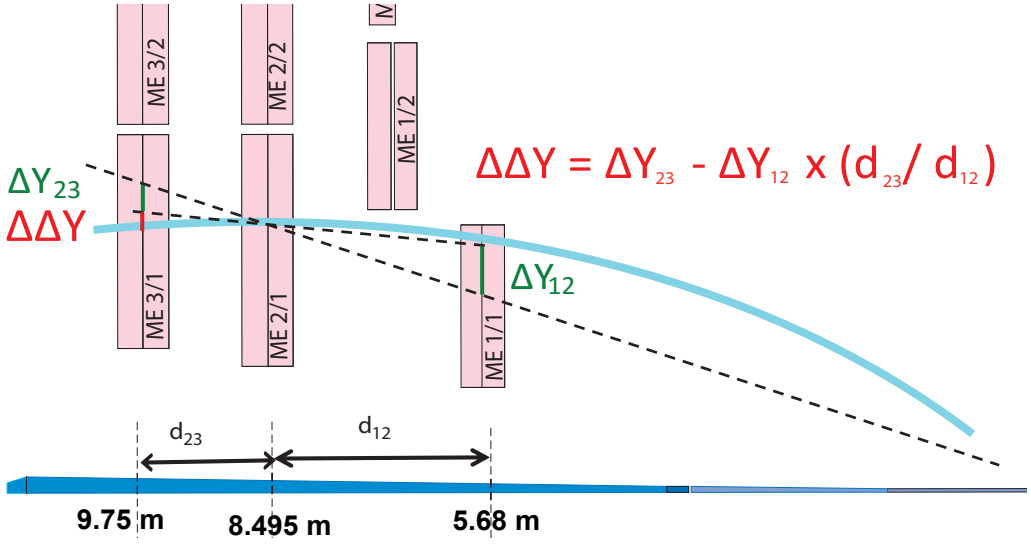

Fig. IV.6. Illustration and definition of the DeltaDeltaY variable used in the position alignment algorithm. Note, that bending of the prompt low p_T muon trajectory actually occurs in the plane transverse to the beam line and not in the longitudinal plane as shown in this drawing. We chose to present it this way to help readers get an intuitive feeling of the procedure used to measure muon momentum.

The dashed lines in Fig. IV.6 form similar triangles that need to be scaled up by the distances between the stations ME1/1 and ME2/1, named d_{12} and the distance between ME2/1 and ME3/1, named d_{23} in the figure. Then we can extrapolate the expected ΔY_{23} and compare it with the actual position of the hit.

The algorithm needs to know the distances d_{12} and d_{23} in order to calculate the scaling factors. Due to the construction of the Muon Endcap stations, such distances are not constant over the entire subsystem. Contiguous chambers are staggered to increase acceptance, hence their positions are alternated between ”odd” and ”even” chambers, following the standard CMS enumeration. Fig. IV.7 shows the disposition for the ME stations.

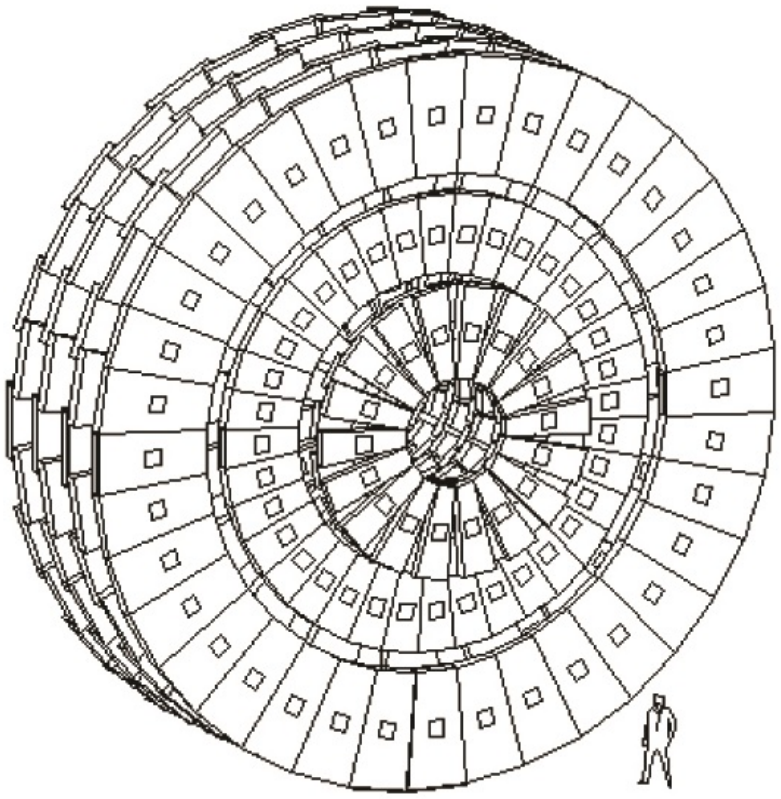

Fig. IV.7. CMS Endcap chamber distribution diagram showing the staggering between ”odd” and ”even” chambers.

Each one of the last three ME stations are 20° chambers that are staggered in a way that odd chambers in ME2/1 always face odd chambers in ME3/1 and even chambers in ME2/1 always face even chambers in ME3/1. However, ME1/1 is a 10° station oriented so that, both an even and an odd ME1/1 chambers are in front of a ME2/1 chamber. We have to individually treat each of the following combination of chambers that muon passed through the following cases:

- Even Chambers in ME1/1 - Even Chambers in ME2/1 and ME3/1.
- Even Chambers in ME1/1 - Odd Chambers in ME2/1 and ME3/1.
- Odd Chambers in ME1/1 - Even Chambers in ME2/1 and ME3/1.
- Odd Chambers in ME1/1 - Odd Chambers in ME2/1 and ME3/1.

It is still possible to have a muon crossing an odd chamber in ME2/1 and an even chamber in ME3/1 but that situation is very rare and will be addressed when developing the final version of this algorithm. The corresponding distances ratios, d_{23}/d_{12} are:

- Even Chambers in ME1/1 - Even Chambers in ME2/1 and ME3/1. $d_{23}/d_{12} = 0.5675$
- Even Chambers in ME1/1 - Odd Chambers in ME2/1 and ME3/1. $d_{23}/d_{12} = 0.3116$
- Odd Chambers in ME1/1 - Even Chambers in ME2/1 and ME3/1. $d_{23}/d_{12} = 0.65$
- Odd Chambers in ME1/1 - Odd Chambers in ME2/1 and ME3/1. $d_{23}/d_{12} = 0.3612$

We can plot ΔY_{23} vs ΔY_{12} in order to get the proper measurements and compare them to the expected values. Such calculations are done in Fig. IV.8 where a good agreement between the theory and the experimental measurements have been achieved.

Once we know the corresponding scale factor, we can compare the variable $\Delta\Delta Y$ with the p_T. However, as it was shown in Fig. II.2, the magnetic field is not constant nor uniform in the Endcap Region. Especial care needs to be taken in order to compensate for this change. For the purpose of our studies, we will segment the Endcap region in slices of 0.2 η, regions, so that variations in

the magnetic field configuration within each slice are relatively small, starting from η = 1.6 all the way up to η = 2.4.

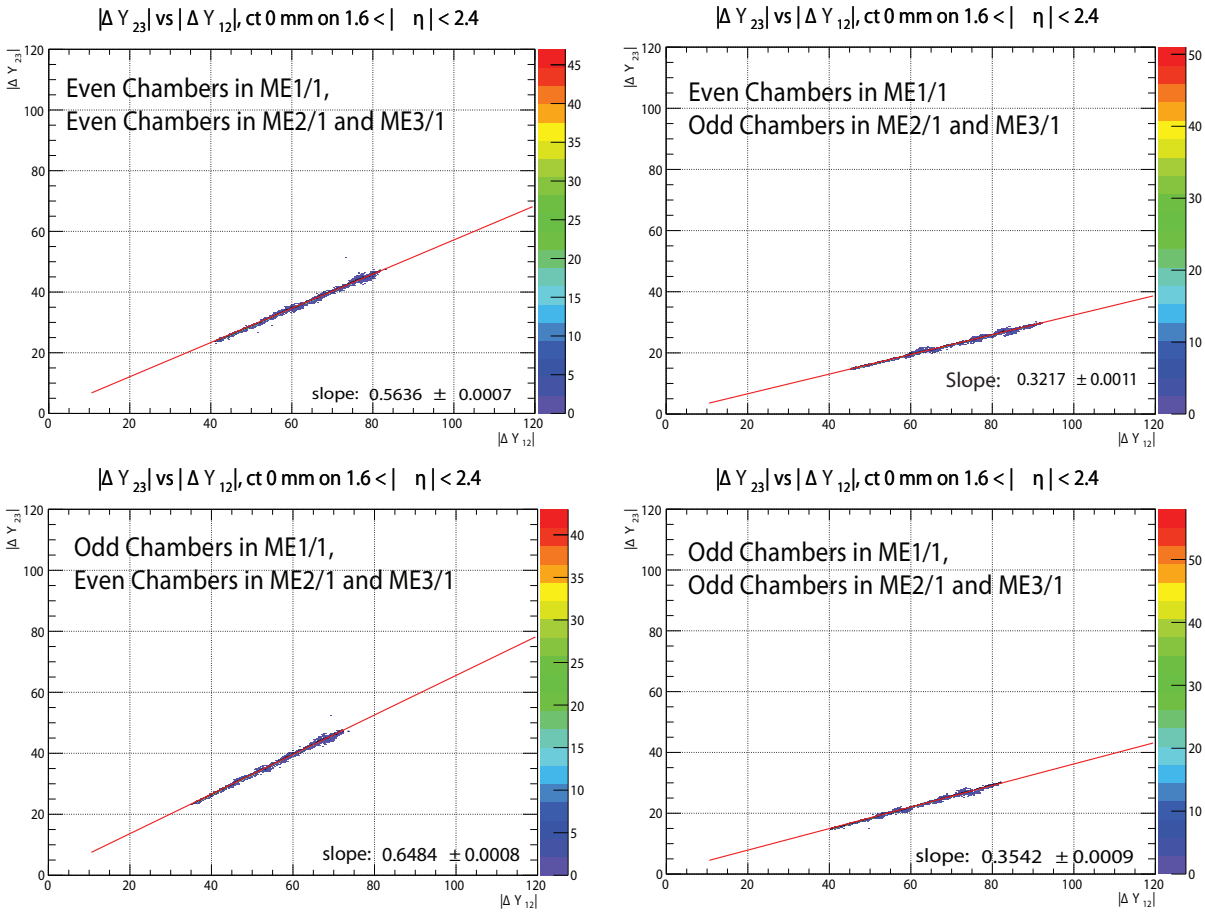

Fig. IV.8. ΔY_{23} vs ΔY_{12} for all of the chamber type combinations cases listed above. The slopes represent the measured values of d_{23}/d_{12} and are in good agreement with the theoretical values.

Using the combination for Odd Chambers in ME1/1, Even Chambers in ME2/1 and ME3/1 as an example, we can calculate the relationship between $\Delta\Delta Y$ and p_T in the η slices that we have selected and observe the reconstruction efficiency for this algorithm. The results are displayed in Fig. IV.9.

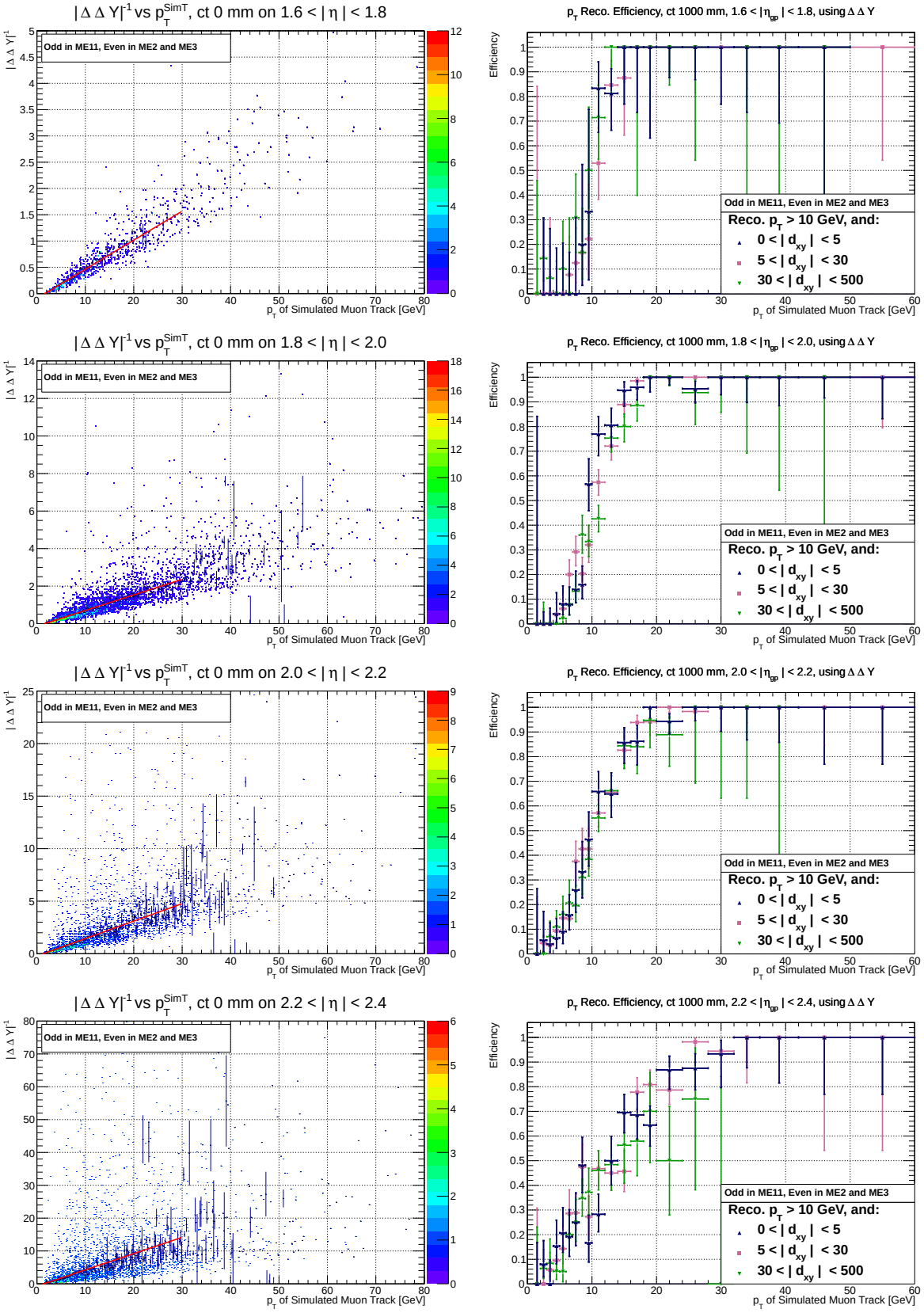

Fig. IV.9. $\Delta\Delta Y$ vs p_T (left) and p_T reconstruction efficiency (right) for all of the η slices between 1.6 and 2.4 for different ranges of the impact parameter.

It is evident that the algorithm was able to reconstruct the p_T for muons regardless of their displacement. After implementing correct treatment of each of the even/odd chamber combinations in the respective η slices, we calculate the efficiency for a muon to pass a minimum threshold requirement $p_T > 20$ GeV as a function of its true transverse momenta, for different ranges of the impact parameter. Fig. IV.10 shows the efficiency confirming that our algorithm correctly reconstructs the transverse momenta of muons regardless of their impact parameter.

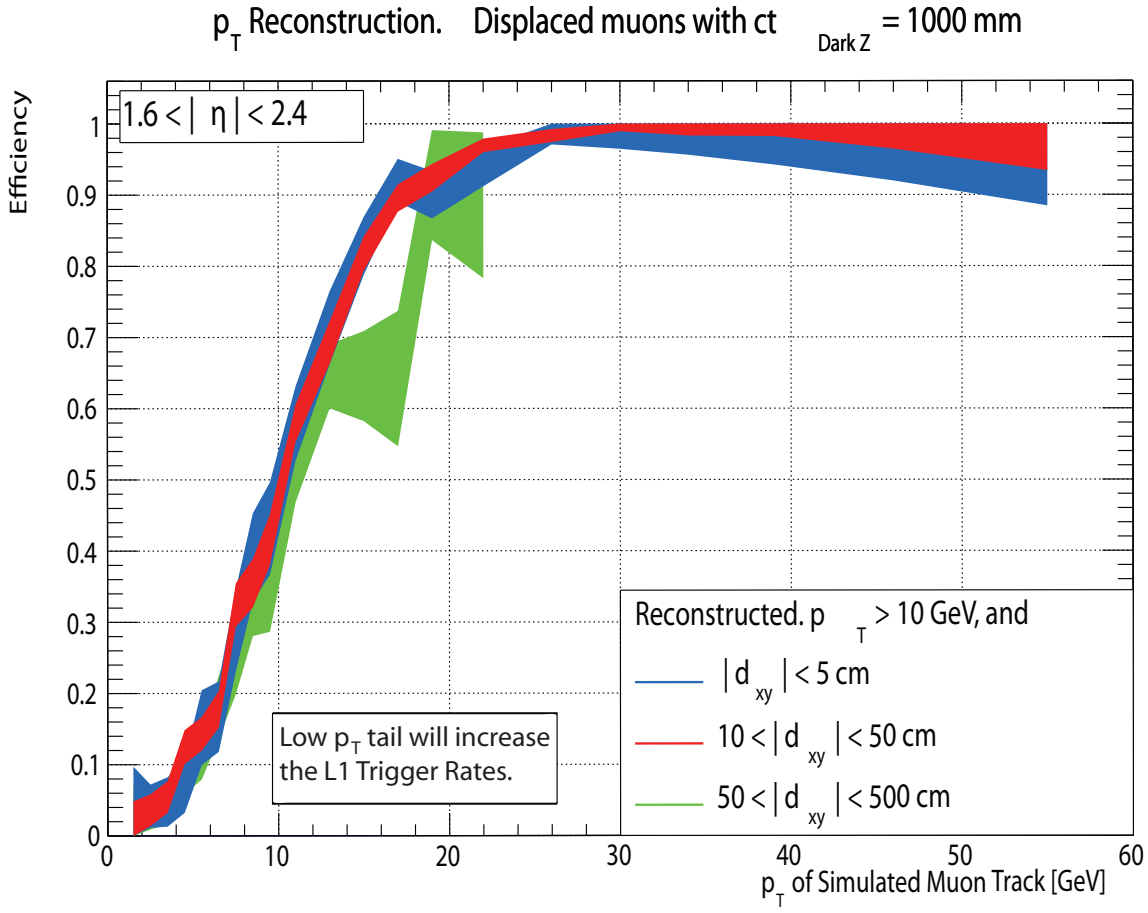

Fig. IV.10. Reconstruction Efficiency for a muon to pass a minimum threshold requirement $p_T > 20$ GeV as a function of its true transverse momenta, for different ranges of the impact parameter.

However, one should note that the efficiency exhibits a tail towards the low p_T seen in Fig. IV.10. If left untreated, such tail in momentum resolution will lead to significant rates, which may exceed allocation of the available L1 bandwidth to the muon trigger. In order to improve the algorithm, we will turn to angular variables and show that they can be used to shape the turn on efficiency curve and make it steeper, as well as it allows reducing the tail towards low p_T. A possible additional measurement can be defined as with the help of Fig. IV.11.

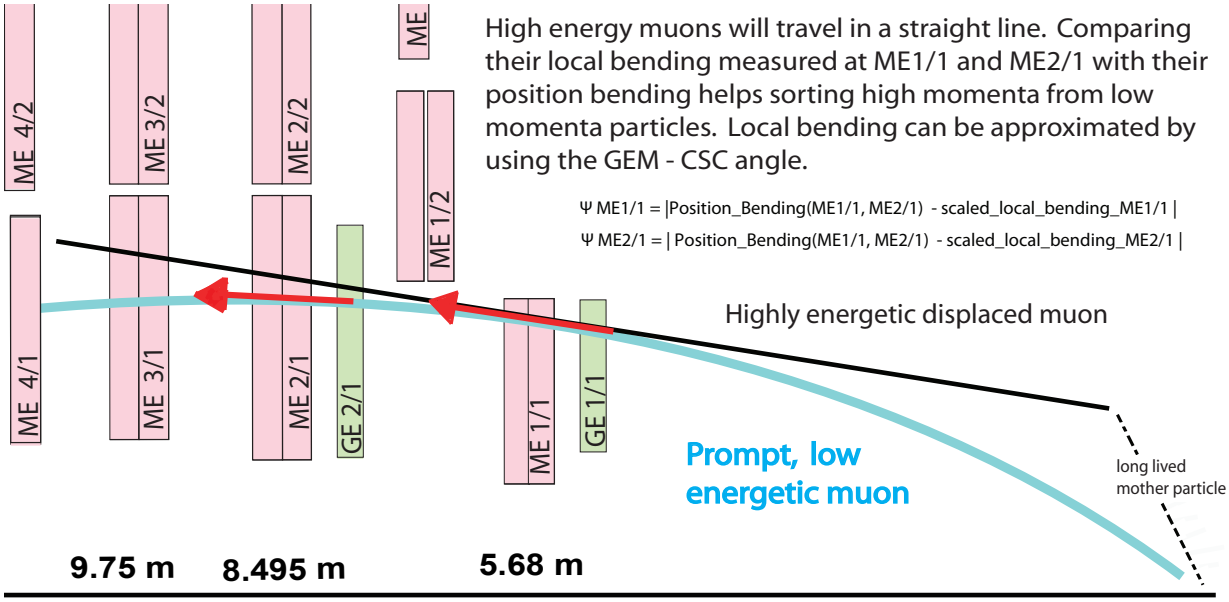

Fig. IV.11. Illustration of the additional requirement to shape the turn on curve on Fig. IV.10. Note, that bending of the prompt low p_T muon trajectory actually occurs in the plane transverse to the beam line and not in the longitudinal plane as shown in this drawing. We chose to present it this way to help readers get an intuitive feeling of the procedure used to measure muon momentum.

We can use a measurement similar to the one used in the Barrel region but modifying it to use the good position resolution in the CSC chambers. We defined the following quantities:

$$\Psi_{ME1/1} = |\Delta\phi(ME1/1, ME2/1) - scaled\_local\_bending\_ME1/1|$$
$$\Psi_{ME2/1} = |\Delta\phi(ME1/1, ME2/1) - scaled\_local\_bending\_ME2/1|$$

The first quantity, $\Delta\phi$ position is the variable used for the current algorithm to measure p_T. The value of $scaled\_local\_bending$ refers to the measurement of the angular direction in either ME1/1 or ME2/1, scaled by the correct factor. We can plot the quantity $\Delta\phi$ vs CSC local bending to get the proper scale factor. Using the same classes of possible chamber combinations, i.e.: Odd Chambers in ME1/1 and Even Chambers in ME2/1 and ME3/1, the correlation between $\Delta\phi$ position and local bending is shown in Fig. IV.12 The slope seen in the plot provides the measurement of the scale factor required to relate $\Delta\phi$ position with the local bending angle.

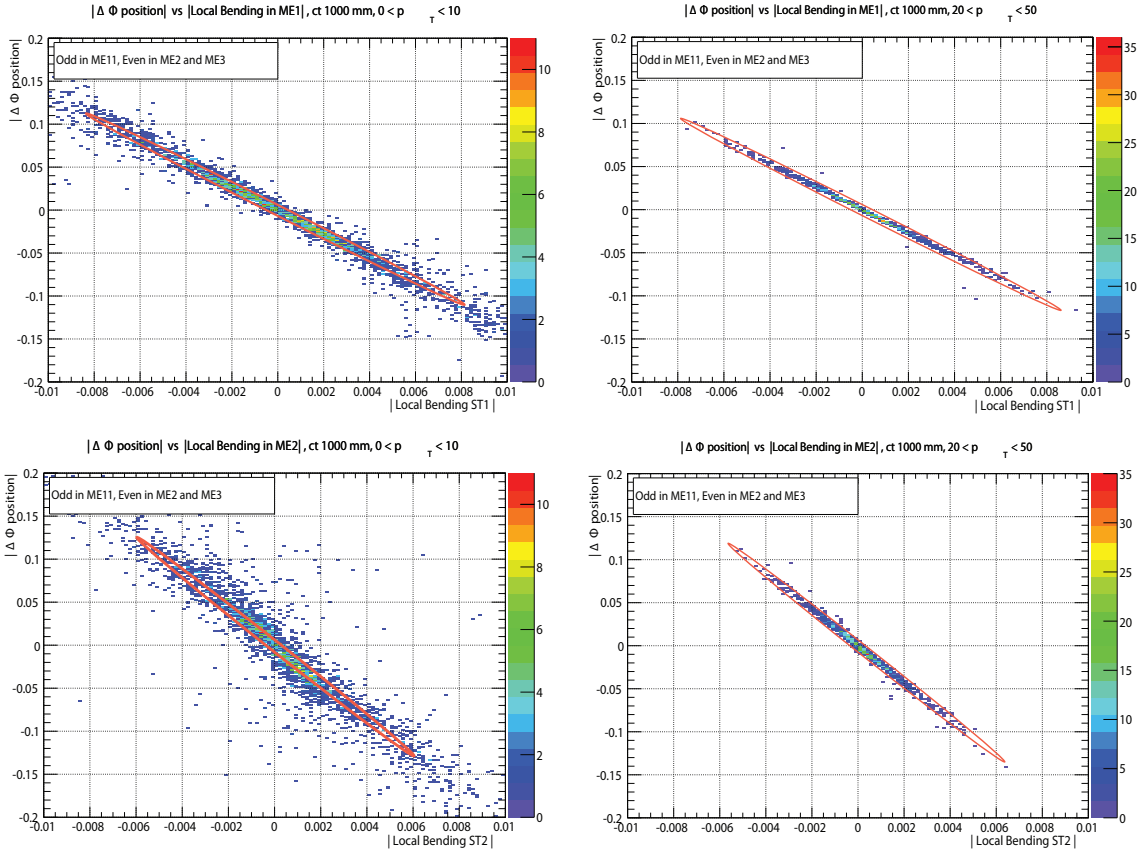

Fig. IV.12. $\Delta\phi$ position vs. local bending in ME1/1 (top) and ME2/1 (bottom) for low p_T (left) and high p_T muons (right). One can see that higher p_T muons show a good correlation between the variables, while soft muons shows a significant scatter. A simple ellipse cut would allow to improve the behavior of the turn on curve by maintaining high efficiency for high p_T muons while reducing the fraction of soft muons passing such cut.

Notice that in Fig. IV.12 we can also select high p_T muons by applying a cut in the plot so that only dots near the perfect straight line are selected. In order to optimize such additional cut, we need to study the distribution of $\Psi_{ME1/1}$ and $\Psi_{ME2/1}$ for different p_T ranges so that we can select the appropriate values for the cut to reject low p_T muons and reduce the tail that was present on Fig. IV.10. Fig. IV.13 shows the distributions for these variables for low p_T and high p_T displaced muons.

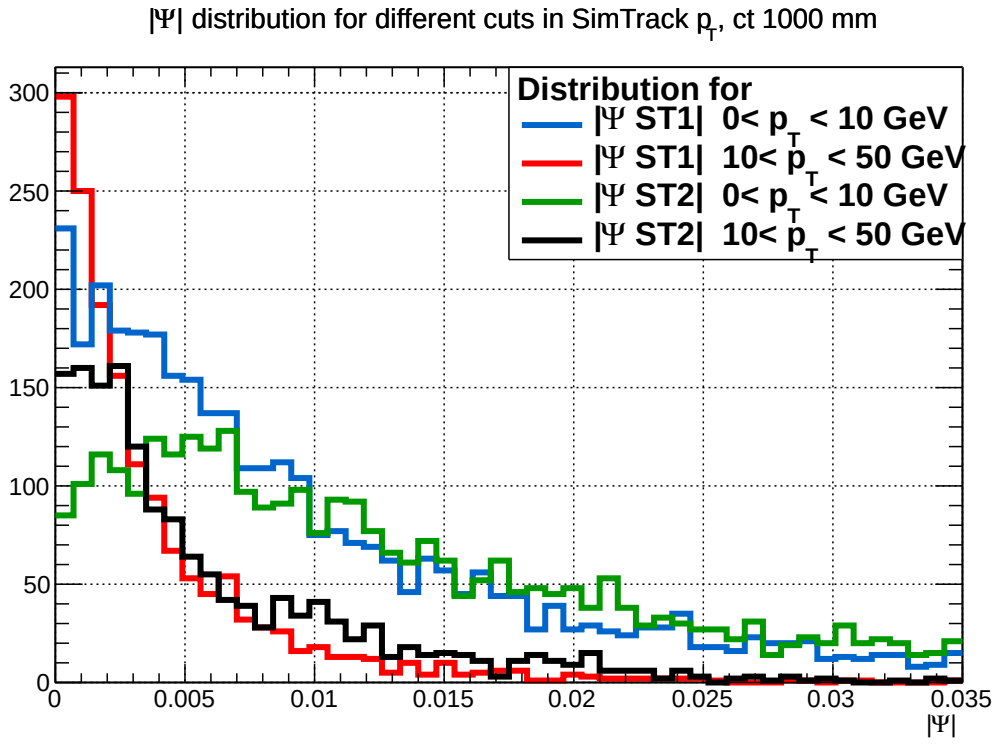

Fig. IV.13. $\Psi_{ME1/1}$ and $\Psi_{ME2/1}$ distribution for "high p_T" defined as $p_T > 20$ GeV, and "low p_T " defined as $0 < p_T < 10$ GeV.

From Fig. IV.13, we will select the values of $\Psi_{ME1/1} < 0.008$ and 0.006 and $\Psi_{ME2/1} < 0.012$ and 0.008. The impact of these additional cuts on the reconstruction efficiency including the p_T requirement are shown in Fig. IV.14.

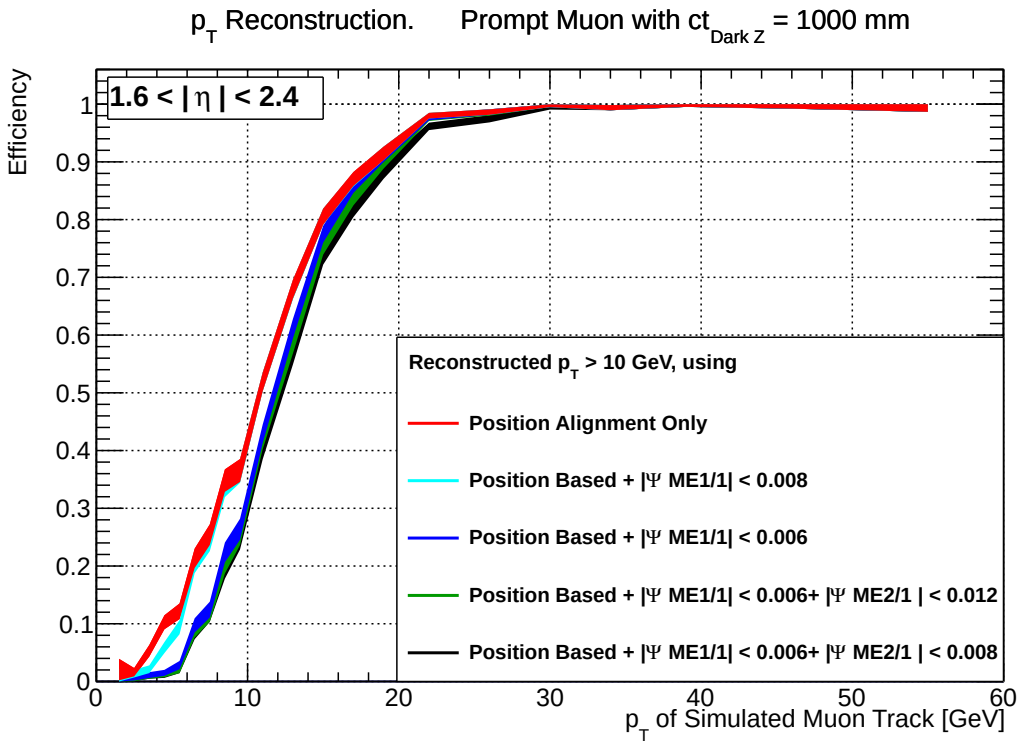

Fig. IV.14. Impact on the Reconstruction Efficiency by applying the additional $\Psi_{ME1/1}$ and $\Psi_{ME2/1}$ cuts, successfully reducing the low p_T tail.

Fig. IV.15 shows the effect on the L1 Trigger Rate. Adding a requirement on $\Psi_{ME1/1}$ helps to reduce the trigger rate down by a factor of 8, and an additional requirement on $\Psi_{ME2/1}$ further reduces the rates down by a factor of 3. The total combined Trigger Rate reduction is on the order of 25, with the achievable trigger rate of the order of 10 kHz for the p_T threshold of 20 GeV, which is close to the target range.

While we have demonstrated the viability of the proposed algorithm for the HL-LHC regime, it requires the muon system to provide a sufficiently precise measurement of the direction of the muon candidate within a single station. This is a challenge for the existing muon system, especially in the most forward region, as the thin CSC detectors do not provide a sufficient lever arm for a precision measurement of the muon direction. This challenge will be resolved with the proposed upgrade of

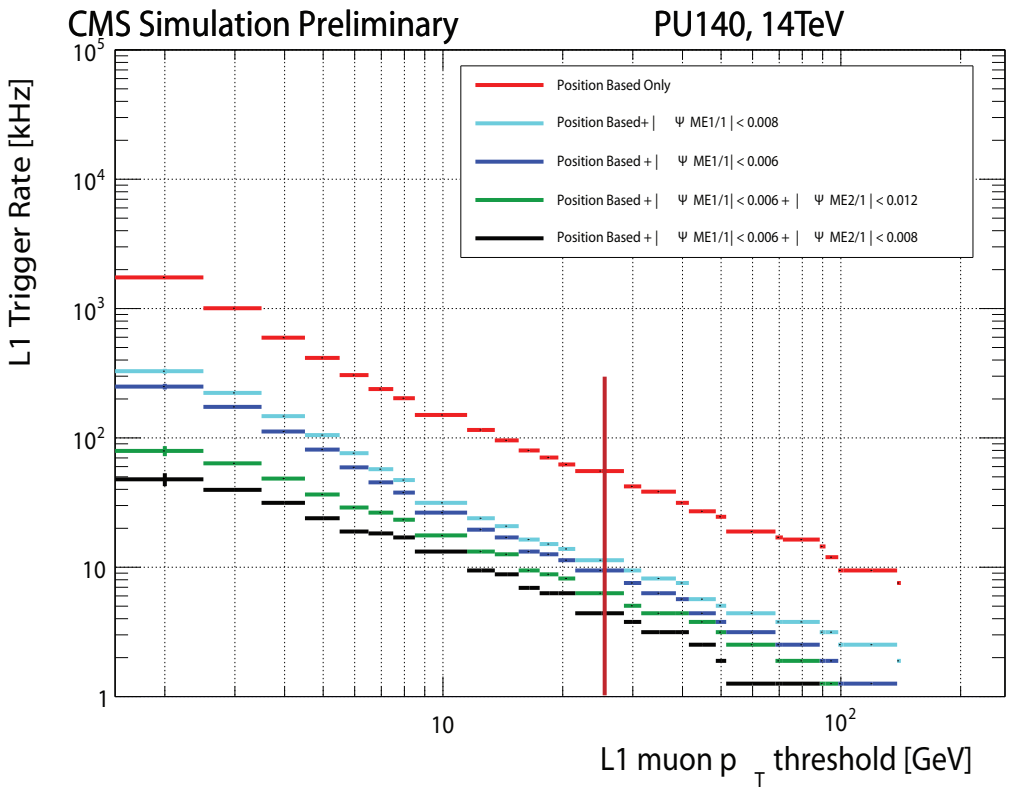

Fig. IV.15. Impact on the Trigger Rates by applying the additional $\Psi_{ME1/1}$ and $\Psi_{ME2/1}$ cuts. Reducing the low p_T tail helps reducing the Trigger Rates.

the CMS muon system to install additional muon chambers utilizing Gas Electron Multiplication (GEM) principle. The proposed GEM stations GE1/1 and GE2/1 will complement existing CSC chambers in stations ME1/1 and ME2/1 by creating effective "large lever arm" detectors capable of accurate measurement of the muon direction using muon hits in the pairs of CSC and GEM chambers. The upgrade will provide two measurements of muon direction, which meets the minimal requirements for Implementing the proposed muon trigger algorithm and is critical requirement for the CMS ability to successfully trigger on muons with substantial impact parameter in the high luminosity era.

Fig. IV.11 and Fig. II.1 illustrates the position of GE1/1 and GE2/1 inside the muon system, where the desired angles can be approximated by the difference in position ϕ coordinates that are left on the GEM-CSC chambers by a traversing muon. The large lever arm provided by the GEM-CSC combination allows for further background rejection and might be combined with the existing algorithm to provide an additional level of redundancy and precision.

The region between $\eta = 1.1$ and $\eta = 1.6$ is impregnated by a magnetic field that is large enough to provide a significant bending, allowing for the usage of the CSC chambers alone in this algorithm but with loose cuts in the angular measurements.

CHAPTER V

CONCLUSIONS

Muons coming from decays of long-lived particles are important signatures in searches for physics beyond the Standard Model. Current selection of displaced muons by the CMS trigger system has been identified as a weak point. If nothing is done, CMS can become completely blind to possible signatures of new physics manifesting themselves through production of long lived particles.

We have proposed a new algorithm able to reconstruct the transverse momenta of muons regardless of their originating position. The algorithm solves the problem that arises when a neutral particle is formed in the collision and decays into muons after a non vanishing distance without interfering with the reconstruction of muons coming directly from the collision point without displacement.

The performance of the proposed algorithm is studied without taking into account inefficiencies in the detector electronics and resolution. While a significant additional tuning of the algorithm will be necessary before it can be implemented, these conceptual level studies show that such trigger design is possible.

REFERENCES

[1] S.L. Glashow (1961). *Partial-symmetries of weak interactions*. Nuclear Physics 22 (4). p. 579–588

[2] S. Weinberg (1967). *A Model of Leptons*. Physical Review Letters 19 (21). p. 1264–1266

[3] A. Salam (1968). N. Svartholm, *ed. Elementary Particle Physics: Relativistic Groups and Analyticity*. Eighth Nobel Symposium. Stockholm: Almquvist and Wiksell. p. 367

[4] F. Englert, R. Brout (1964). *Broken Symmetry and the Mass of Gauge Vector Mesons*. Physical Review Letters 13 (9). p. 321–323.

[5] P.W. Higgs (1964). *Broken Symmetries and the Masses of Gauge Bosons.* Physical Review Letters 13 (16). p. 508–509.

[6] G.S. Guralnik, C.R. Hagen, T.W.B. Kibble (1964). *Global Conservation Laws and Massless Particles*. Physical Review Letters 13 (20). p. 585–587.

[7] CMS Collaboration *Observation of a new boson at a mass of 125 GeV with the CMS experiment at the LHC* . Phys. Lett. B 716 (2012). p. 30 - 61. arXiv:1207.7235

[8] ATLAS collaboration (2012). *Observation of a New Particle in the Search for the Standard Model Higgs Boson with the ATLAS Detector at the LHC*. Physics Letters B 716 (1).

p. 1–29. arXiv:1207.7214

[9] K.A. Olive et al., Chin. Phys. C, 38, 090001. Particle Data Group. 2014.

[10] Inquiring Minds, *What is the world made of?* 2014: Fermilab. http://www.fnal.gov/pub/science/inquiring/matter/madeof/. 2016

[11] The Large Hadron Collider, *CERN Accelerator Complex*. TE-EPC Collaboration. Website: http://te-dep-epc-oms.web.cern.ch/te-dep-epc-oms/operation-en/operation.stm 2016.

[12] Mans, J. et. al., *CMS Technical Design Report.* CMS Collaboration. CERN-LHCC-2012-015 / CMS-TDR-010.

[13] S. Chatrchyan el at, *The CMS experiment at the CERN LHC.* The CMS Collaboration, J. Instrum 3 (2008) S08004

[14] A. Castaneda et al. *Potential Impact of a New GEM Based Detector on CMS Triggering*. CSC GEM Collaboration, October 2013. arXiv:1310.2074

[15] CMS Software and Physics, Reconstruction and Selection (PRS) Projects, *Physics Technical Document Reading. Volume 1: Detector Performance and Software* 2006. CERN.

[16] Spicas Paris et. al., *The TriDAS Project: The Level-1 Trigger - Technical Design Report* . CMS Collaboration. December, 2000.

[17] Sjöstrand Torbjörn et. al., *An Introduction to PYTHIA 8.2*, Comput. Phys. Commun. 191 (2015). p. 159-177. arXiv:1410.3012

[18] Colaleo, A; Safonov, A; Sharma, A; Tytgat, M. *CMS Technical Design Report for the Muon Endcap GEM Upgrade.* CERN-LHCC-2015-012 ; CMS-TDR-013